Polarimetric remote sensing of aerosols over land

F. Waquet,[1,2] B. Cairns,[3] K. Knobelspiesse,[1] J. Chowdhary,[1] L. D. Travis,[3] B. Schmid,[4] and M. I. Mishchenko[3]

Received 17 June 2008; revised 13 September 2008; accepted 10 October 2008; published 9 January 2009.

[1] We present a new approach to retrieve the aerosol properties over land that uses accurate polarization measurements over a broad spectral (410–2250 nm) and angular (±60° from nadir) ranges. The approach uses longer wavelength observations to accurately estimate the surface effects, and it is incorporated into an optimal estimation framework for retrieving the particle number density and a detailed aerosol microphysical model: effective radius, variance, and complex refractive index. A sensitivity analysis shows that the uncertainties in aerosol optical thickness (AOT) increase with AOT while the uncertainties in the microphysical model decrease. The uncertainty in the single scattering albedo (SSA) is notably less than 0.05 by the time the AOT is greater than 0.2. We find that calibration is the major source of uncertainty and that perfect angular and spectral correlation of calibration errors reduces the uncertainties in retrieved quantities. Finally, we observe that shorter wavelength (<500 nm) observations are crucial for determining the aerosols vertical extent and imaginary refractive index from polarization measurements. The retrieval approach is tested under pristine and polluted conditions using observations made by the Research Scanning Polarimeter during the Aerosol Lidar Validation experiment and over California Southern wild fires. In both cases we find that the retrievals are within the combined uncertainties of the retrieval and the Aerosol Robotic Network Cimel products and Total Ozone Mapping Spectrometer Aerosol Index. This demonstrates the unique capability of polarization measurements to accurately retrieve AOTs under pristine conditions and provide estimation of the SSA at higher AOTs.

Citation: Waquet, F., B. Cairns, K. Knobelspiesse, J. Chowdhary, L. D. Travis, B. Schmid, and M. I. Mishchenko (2009), Polarimetric remote sensing of aerosols over land, *J. Geophys. Res.*, *114*, D01206, doi:10.1029/2008JD010619.

1. Introduction

[2] Aerosols affect the climate of the Earth primarily by changing the amount of solar radiation that the Earth system absorbs. Indeed, aerosols can either reduce the amount of solar radiation that is absorbed by the Earth system, or even increase it [*Haywood and Shine*, 1995]. Their net radiative effect may therefore be to compensate for increases in greenhouse gases or to exacerbate their effects. The current and historical magnitude, and even the sign regionally, of this net radiative forcing by aerosols is uncertain because the size, composition and burden of aerosols is not very well known [*Hansen et al.*, 2005a; *Chung and Seinfeld*, 2005; *Intergovernmental Panel on Climate Change*, 2007] and also because aerosols can affect the formation and dissipation of clouds [*Lohman and Feichter*, 2005]. It is these facts, together with increasing concerns [*Rosenzweig et al.*, 2008] about the current and potential future effects of greenhouse gases that has raised the level of importance of providing more accurate knowledge of the global distribution and microphysical properties of aerosols. The main purpose of obtaining such knowledge is so that the radiative forcing of the Earth can be defined with sufficient accuracy to evaluate model predictions of climate change against the observed state of the climate and secondarily to provide a detailed climatology of aerosols that can be used to evaluate and improve the chemical/aerosol transport models that are being used to make climate predictions [*Ramanathan et al.*, 2001, *Mishchenko et al.*, 2004; *Hansen et al.*, 2005b]. The only way to obtain this knowledge globally is using satellite based remote sensing and it is this topic that is the subject of this paper.

[3] Although lidar systems can make observations of aerosols with similar capabilities over both land and ocean and clearly provide the best approach to determining the vertical distribution of aerosols, those systems, and in particular space-borne ones, have a limited capability to determine the composition and size of aerosols, and this leads to substantial uncertainties in their estimates of the total burden of aerosols without some prior knowledge of aerosol type being available [*Ackermann*, 1998; *Barnaba and Gobbi*, 2004; *Cattrall et al.*, 2005]. For passive remote sensing systems the problem of retrieving aerosols over oceans is substantially easier than over land. This is because

[1]Department of Applied Physics and Applied Mathematics, Columbia University, New York, New York, USA.
[2]Now at Laboratoire d'Optique Atmosphérique, Université des Sciences et Technologies de Lille, Villeneuve-d'Ascq, France.
[3]NASA Goddard Institute for Space Studies, New York, New York, USA.
[4]Pacific Northwest National Laboratory, Richland, Washington, USA.

Copyright 2009 by the American Geophysical Union.
0148-0227/09/2008JD010619

variations in the reflectance of the ocean can be reasonably well understood in terms of the variability of a single parameter, the chlorophyll concentration, which allows the aerosol properties and chlorophyll concentration to be retrieved simultaneously [*Chowdhary et al.*, 2006; *Stamnes et al.*, 2003], or spectral bands can be used that are immune to variations in the chlorophyll concentration [*Kaufman et al.*, 1997a; *Martonchik et al.*, 1998; *Kahn et al.*, 2001]. The nature of the remote sensing problem over oceans is therefore quite well understood in terms of the required accuracy of the measurements [*Mishchenko and Travis*, 1997a; *Mishchenko et al.*, 2004], the importance of having a broad spectral range [*Tanré et al.*, 1996], the value of having multiangle measurements [*Martonchik et al.*, 2002] and the benefits of including polarization measurements [*Mishchenko and Travis*, 1997b; *Cairns et al.*, 1997; *Deuzé et al.*, 2001; *Chowdhary et al.*, 2001, 2002; *Lebsock et al.*, 2007].

[4] Over land the aerosol retrieval problem is somewhat more difficult because typical variations in time and space of the land surface reflectance are substantially larger than the reflectance caused by aerosols. However, the sources of aerosols generated by human activities are predominantly over land and it is also over land (and clouds) that aerosols can cause a net increase in the amount of solar radiation absorbed by the Earth system, because, if they are absorbing, they can make the Earth appear darker than is the case for an atmosphere in which there are no aerosols [*Haywood and Shine*, 1995]. The capability to use remote sensing methods to retrieve aerosol properties over land is therefore an important aspect of providing a better understanding of the radiative forcing caused by aerosols.

[5] The retrieval of aerosol properties over land was initially performed over dense dark vegetation for which the uncertainties in surface reflectance are the least and was restricted to an estimate of the aerosol optical thickness (AOT) [*Kaufman et al.*, 1997a; *Zagolski et al.*, 1999]. This approach was extended to a wider variety of surface types based on the empirical observation that the dependence of surface reflectance in the visible spectral domain is closely linked to that in the short-wave infrared (SWIR) for many surface types [*Kaufman et al.*, 1997b; *Chu et al.*, 2002], although the primary retrieved quantity is still the AOT with the aerosol microphysical model being prescribed regionally [*Remer et al.*, 2005]. An alternative method for determining aerosol properties over land is to use multiangle measurements where it can be assumed that the relative angular variation in the measurements has a negligible spectral dependence even as the absolute magnitude of the reflectance changes [*Flowerdew and Haigh*, 1995; *Veefkind et al.*, 1998; *North*, 2002]. High spatial resolution multiangle measurements over heterogeneous surfaces can also be used to separate the surface and atmospheric contributions to the radiances observed at the TOA [*Martonchik et al.*, 2002] even over bright deserts [*Martonchik et al.*, 2004]. The final radiance only method that has been used to retrieve AOT over land uses UV observations for which the land surface albedo is both dark and stable [*Torres et al.*, 1998]. The accuracy of these AOT retrievals as compared to ground-based sunphotometers is of order 20–30% at high optical depths [*Remer et al.*, 2005; *Abdou et al.*, 2005; *North*, 2002; *Torres et al.*, 2002] with the accuracy at lower optical depths being very dependent on the particular method and the surface type. Moreover, these radiance-based methods provide very limited capability to determine the aerosol size and composition that is present, with discrepancies in the retrieved AOT and sunphotometer measured AOT frequently being ascribed to erroneous aerosol model assumptions [*Chu et al.*, 2002; *Kahn et al.*, 2005].

[6] In this paper we evaluate the use of polarization observations over land, that have a broad spectral (410–2250 nm) and angular (±60° from nadir) range, in order to retrieve not just the AOT, but also an aerosol model consisting of a size distribution and a complex refractive index. This allows most assumptions about the aerosol composition and size, required by other methods, to be eliminated thereby also reducing biases in the retrieved AOT. Previous authors [*Deuzé et al.*, 2001; *Lebsock et al.*, 2007] have performed analyses and developed retrieval approaches that are applicable to the polarized observations in two spectral bands at 670 and 865 nm provided by POLDER [*Deschamps et al.*, 1994]. The Research Scanning Polarimeter (RSP) aircraft instrument [*Cairns et al.*, 1999, Appendix A] and Aerosol Polarimetry Sensor (APS) planned for launch in 2009 as part of the NASA Glory mission [*Mishchenko et al.*, 2007] both provide polarized observations in seven spectral bands that are predominantly free of gaseous absorption at 412, 443 (469), 555, 672, 865, 1610 (1590) and 2250 nm (where parenthetic values refer to RSP bands that differ from APS). In section 2 we describe how this broad spectral range provides a substantially greater capability to characterize and eliminate the effects of the surface on the observed polarized radiance than is possible with the POLDER approach. This information is then incorporated into an application of the optimal estimation method (section 3) [*Rodgers*, 2000] that includes realistic instrument calibration and noise [*Cairns et al.*, 1999, Appendix B] to evaluate the sensitivity of the measurements to the various aerosol retrieval parameters (section 4) including the pressure level of the top of the aerosol layer. We also demonstrate the importance of short wavelength observations ($\lambda < 555$ nm) in effectively constraining the complex refractive index of accumulation mode particles. In section 5 we apply the method to a set of field experiment observations performed with the RSP that provide a test of the realism of both the low and high aerosol optical depth regimes. In section 6 we summarize our results and present our conclusions regarding the capabilities of polarimetric remote sensing over land and what is required of a polarimetric sensor in order for these capabilities to be realized.

2. Modeling of the Measurements

2.1. Modeling of the Radiation Field

[7] The intensity and state of polarization of light can be described by the (4 × 1) Stokes vector **I** which has the four Stokes parameters I, Q, U and V as its components [*Hansen and Travis*, 1974]:

$$\mathbf{I} = (I, Q, U, V)^T, \tag{1}$$

where T indicates a transposed vector and the Stokes parameters are defined with respect to a certain plane of reference and have units of W m^{-2} nm^{-1} when being used to

define an irradiance and units of W m^{-2} nm^{-1} sterad^{-1} when defining a radiance. The parameter I describes the intensity of the radiation field, Q and U describe the magnitude and orientation of the linear polarization and V describes the helicity and magnitude of the circular polarization.

[8] Let $\mathbf{I_0}$ denote a specific intensity vector of a unidirectional beam of sunlight illuminating a plane parallel atmosphere from the direction of (θ_s, φ_s). θ_s and φ_s are respectively the solar zenith and azimuth angles. If the atmosphere is bounded below by a reflecting surface, the upward Stokes vector $\mathbf{I_u}$ at the top of the atmosphere in the direction (θ_v, φ_v) can be written as follows,

$$\pi \mathbf{I_u}(\lambda, \mu_s, \mu_v, \varphi_s - \varphi_v) = \mu_s \mathbf{R}^{Atm+Surf}(\lambda, \mu_s, \mu_v, \varphi_s - \varphi_v) \cdot \mathbf{I_0}(\lambda, \mu_s, \varphi_s), \quad (2)$$

where λ indicates the spectral dependence of the quantity. μ_s and μ_v are respectively the cosines of the solar and view zenith angles. $\mathbf{R}^{\mathrm{Atm+Surf}}$ is the (4 × 4) reflection matrix of the surface-atmosphere system [*Hansen and Travis*, 1974]. The $\mathbf{R}^{\mathrm{Atm+Surf}}$ matrix describes all the scattering processes occurring in the surface-atmosphere system and can be expressed as a function of the reflection and transmission matrices of the atmosphere and the surface reflection matrix. These matrices can be computed for any given atmospheric and surface model using the vector adding/doubling method [*De Haan et al.*, 1987]. Indeed, similar matrices can be calculated for the upwelling and down-welling radiation at any level in the atmosphere allowing the simulation of polarized radiation field for comparison with downward looking aircraft, or ground based upward looking observations.

[9] In order to calculate the multiple scattering properties of any atmosphere using the adding/doubling adding method it is necessary to specify the vertical distribution of scatterers and their scattering properties. We use the molecular optical thickness given by *Hansen and Travis* [1974] with a scale height of 8 km together with a spectrally invariant depolarization of 0.0279 [*Bodhaine et al.*, 1999] to define the scattering properties and vertical distribution of Rayleigh scattering. We assume that the aerosol population can be described by a bimodal size distribution. Each mode (coarse and fine) is described by its own log-normal size distribution given by

$$N(r) = \frac{N_0}{\sqrt{2\pi}\sigma r} \exp\left[\frac{-(\ln r - \ln r_g)^2}{2\sigma^2}\right], \quad (3)$$

where r_g (μm) is the geometric mean radius, σ is the variance and N_0 (μm^{-2}) is the column number density of particles. In the analysis of the retrieval of aerosols over land presented here the particles are considered to be spherical and so all that remains to define their optical properties is the complex refractive index $m_r - im_i$ for each mode. The aerosol optical thickness, τ, and the single scattering albedo, ω_0, can then be defined in terms of the extinction, C_{ext} (μm^2), and scattering, C_{sca} (μm^2), cross-sections of the aerosols as

$$\tau = N_0 C_{ext}$$
$$\omega_0 = {}^{C_{sca}}/_{C_{ext}}. \quad (4)$$

[10] For the convenience of the reader we also note that the commonly used [*Hansen and Travis*, 1974] size distribution parameters of the effective radius, r_{eff}, and effective variance, v_{eff}, are related to the log normal size distribution parameters given in equation (3) by the formulae

$$r_{eff} = r_g \exp\left(\tfrac{5}{2}\sigma^2\right)$$
$$v_{eff} = \exp(\sigma^2) - 1, \quad (5)$$

provided the size distribution is not truncated [*Mishchenko et al.*, 2002]. In the following, the suffixes f and c indicate parameters that respectively belong to the fine and coarse mode. When no specific vertical structure of the atmosphere is given, we consider that the aerosols are homogeneously distributed throughout the two lowest kilometers of the atmosphere.

2.2. Modeling of the Polarized Reflectance

[11] For naturally illuminated scenes the circular polarization is typically several orders of magnitude smaller than the linear polarization. Moreover, the state of linear polarization can be measured without the circular polarization having any significant effect, while the calculation of linear polarization is affected negligibly by neglecting the circular polarization and just using a 3 × 3 approximation to the full 4x4 reflection matrix. In the following, we therefore use the total and polarized reflectances, R and R_p, derived from the Stokes parameters I, Q and U. R is given by

$$R = \pi I / \mu_s I_0, \quad (6)$$

where I_0 is the spectral solar extraterrestrial irradiance (W m^{-2} nm^{-1}). R_p is given by

$$R_p = -\pi Q / \mu_s I_0. \quad (7)$$

Q is the second Stokes parameter defined with respect to the scattering plane (the plane which contains both solar and view directions). The parameter Q is here sufficient to describe the linear polarization since U becomes negligible when the Stokes parameters are defined with respect to the plane of scattering and when the polarized surface reflectance is similar to that caused by Fresnel reflection [*Bréon et al.*, 1995], as discussed in the following. The sign convention used here is that the polarized reflectance is positive (negative) when the direction of polarization is perpendicular (parallel) to the normal to the scattering plane.

2.2.1. Surface Level

[12] Different experimental studies have shown that the surface polarization is mainly generated by single reflection at surface facets (e.g., leaves cuticles, grains of soil). If this is the case, the surface polarized reflectance depends on (1) the Fresnel law (i.e., surface refractive index and refection angle), (2) the surface physical and geometrical properties (e.g., roughness, shadowing, inclination of the leaves etc.), and (3) the viewing geometry. Figure 1 shows an example of polarized reflectances measured at 2.25 μm over a vegetated surface and a bare soil in the Southern Great Plains together with the Fresnel reflectance for those viewing geometries scaled by a coefficient that does not depend on illumination or viewing geometry. The measure-

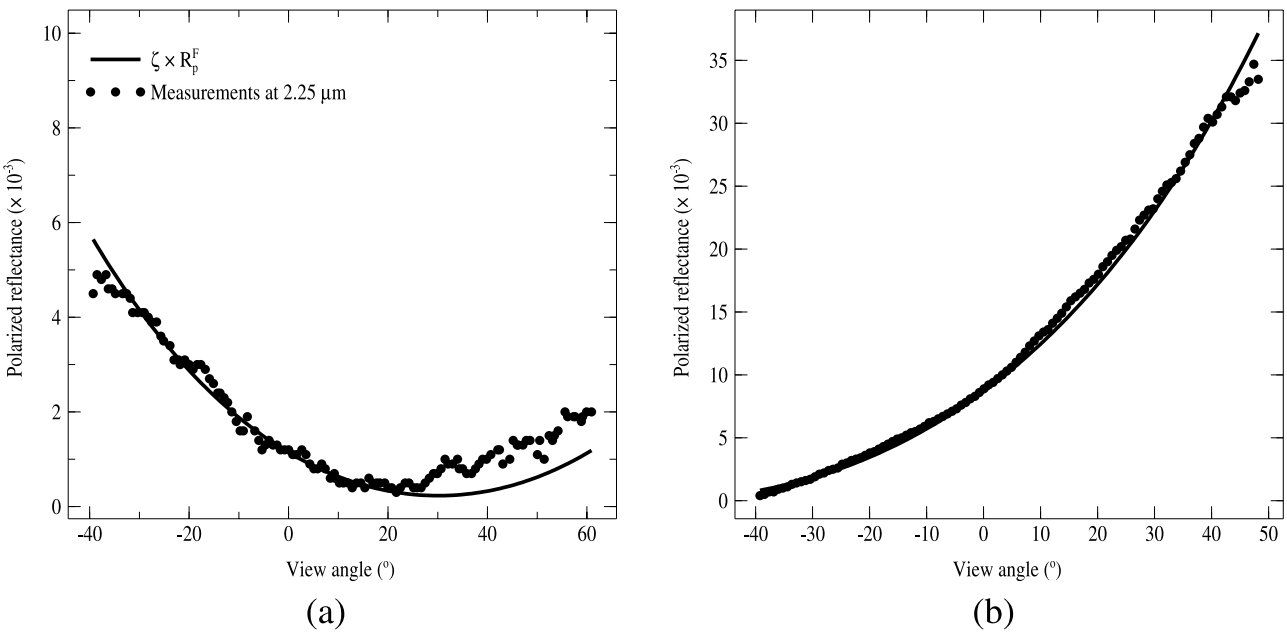

Figure 1. Polarized reflectance measured at 2.25 μm over (a) a vegetated surface and (b) a bare soil (dots). Polarized reflectance generated by the Fresnel reflection (solid line) scaled by a coefficient. Viewing geometry for (a) $\varphi_s - \varphi_v = 45°$ and $\theta_s = 60°$ and (b) $\varphi_s - \varphi_v = 0°$ and $\theta_s = 30°$.

ments for each surface type were performed for different illumination angles (θ_s, φ_s) and for a different viewing plane (φ_v). The effect of the atmosphere is small here with the aerosol optical depth at 2130 nm, as measured by the AATS-14, being 0.05 or less and the measurements can therefore be regarded as being dominated by the direct surface contribution. The polarized reflectances are modeled as follows,

$$R_p^{Surf}(\mu_s, \mu_v, \varphi_s - \varphi_v) = \zeta R_p^F(\gamma). \tag{8}$$

R_p^F is the Fresnel coefficient for polarized light calculated for a surface refractive index of 1.5 that is a value commonly accepted for natural surfaces. γ is the reflection angle that can be expressed as a function of the scattering angle, Θ, by $\gamma = (\pi - \Theta)/2$ with ζ being a coefficient that provides the best fit to the measurements at 2.25 μm.

[13] The coefficient ζ accounts for the intrinsic properties of the surface. In particular, it accounts for the actual surface refractive index being different from that assumed in the model since the polarized reflectance calculated with one refractive index is proportional to a good degree of approximation to that with a different one (this is one of the properties of the Fresnel polarized reflectance). Figure 1 shows that the functional variation of the surface polarization with the viewing and illumination angles can be robustly modeled by only considering the Fresnel reflection, whether the surface is a bare soil or vegetation. Assuming that the azimuth behavior of the surface polarization only depends on the Fresnel law, this model estimated in the plane of observations can be used to predict the surface polarization for any other viewing plane. Such an assumption has been commonly made for the development of surface polarization models [*Bréon et al.*, 1995; *Nadal and Bréon*, 1999] and is also made here. In the following, we improve this simple model by adjusting the ζ factor for each view angle.

[14] Another unusual feature of the surface polarized reflectance is its lack of color. This is theoretically justified by the fact that the real component of the refractive indices of many rocks and the waxes that cover vegetation show a rather flat spectral behavior [*Pollack et al.*, 1973]. Laboratory measurements of the polarized reflectance of a variety of leaves at the Brewster angle also show very weak spectral variation across the visible spectrum from 400 to 900 nm [*Grant et al.*, 1993]. The lack of spectral variation of polarized reflectance has also been born out by airborne measurements over a wide spectral range from the short visible to the middle infrared spectra and for various surface types (e.g., forest, crops, bare soil) [*Cairns et al.*, 2001; *Elias et al.*, 2004; *Waquet et al.*, 2007]. As the effect of the atmosphere is typically very small in the middle-infrared, the model previously defined can be estimated using middle-infrared measurements and then applied to modeling the surface polarization in all spectral bands across the solar spectrum.

2.2.2. Instrument Level

[15] In order to describe the main processes that generate the up-welling polarized reflectance, we provide in equation (9) an approximate expression for the surface-atmosphere reflection matrix viz.,

$$\begin{aligned}\mathbf{R}^{Atm+Surf} &= \mathbf{R}^{Atm} + t_+\mathbf{R}^{Surf}t_- \\ &\quad + \left[\mathbf{T}_+^d\mathbf{R}^{Surf}t_- + t_+\mathbf{R}^{Surf}\mathbf{T}_-^d + \mathbf{T}_+^d\mathbf{R}^{Surf}\mathbf{T}_-^d\right],\end{aligned} \tag{9}$$

in which we have suppressed the dependence of the matrices on the viewing geometry (μ_s, μ_v, $\varphi_s - \varphi_v$) and wavelength for the sake of clarity. The minus (plus) subscripts refers to a downward (upward) direction. $\mathbf{R}^{Atm}$ and $\mathbf{R}^{Surf}$ are respectively the atmospheric and surface

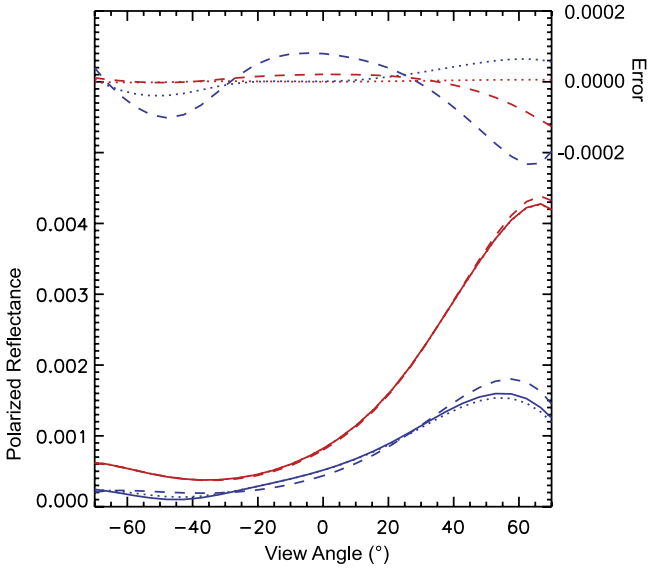

Figure 2. Contribution of the surface polarized reflectance (blue lines) to the TOA polarized reflectance (red lines). Exact calculations (solid lines), calculations without multiple scattering interactions between surface and atmosphere (dotted lines) and calculations performed using direct transmission term and scaling optical thicknesses (dashed lines). The errors on the surface and TOA polarized reflectances are shown in more detail at the top of the figure. Aerosol layer: $r_{eff}^{s} = 0.14$, $v_{eff}^{s} = 0.15$, $r_{eff}^{l} = 2.5$, $v_{eff}^{l} = 0.5$, $m_r^{s} = m_r^{l} = 1.4$, and $\tau_a = 0.1$ at 550 nm. Calculations made for a solar zenith angle of 45°, $\varphi_s - \varphi_v = 45°$ and at a wavelength of 0.55 μm.

reflection matrices. $\mathbf{T}^d$ corresponds to the diffuse transmission matrix of the atmosphere and t is a direct transmission term given by

$$t_{-,+} = \exp\left[-\left(\frac{\tau_{a,\lambda} + \tau_{r,\lambda}}{\mu_{s,v}}\right)\right], \tag{10}$$

where τ_a and τ_r are respectively the aerosol and molecular total optical thicknesses.

[16] Equation (9) is arranged in order to separate the terms that contribute to the observed reflectance into three distinct components. The first term $\mathbf{R}^{Atm}$ describes the contribution of the upwelling light scattered from the atmosphere without interactions with the surface. The second term describes the surface contribution transmitted directly through the atmosphere while the third term, between brackets, models the diffuse interactions between the surface and the atmosphere. An exact expression for $\mathbf{R}^{Atm+Surf}$ would require the inclusion of multiple surface reflections (i.e., multiple scattering interactions between surface and atmosphere).

[17] Figure 2 shows an example of polarized reflectances calculated at the surface and TOA levels (solid lines) and the same quantities calculated when suppressing the process of multiple surface reflections (dots). It is apparent that the contribution of multiple surface-atmosphere interactions to the observed polarization is small at the surface and, since it is attenuated by the atmosphere, is negligibly small at the top of the atmosphere. Note that this process is generally accounted for in our adding-doubling calculations but can, if necessary, be neglected and the surface-atmosphere interaction for polarization can be treated using equation (9) rather than a full adding calculation.

[18] The polarized reflectances measured over land are usually modeled by considering only the up-welling polarized light scattering from the atmosphere and a single reflection off the surface [*Deuzé et al.*, 2001; *Waquet et al.*, 2007]. The polarized reflectance can then be written in the following form,

$$R_{p,\lambda}^{calc}(\mu_s, \mu_v, \varphi_s - \varphi_v) = R_{p,\lambda}^{atm}(\mu_s, \mu_v, \varphi_s - \varphi_v) + t_{+}^{*} R_p^{surf}(\mu_s, \mu_v, \varphi_s - \varphi_v) t_{-}^{*}. \tag{11}$$

In this equation R_p^{atm} is the atmospheric polarized reflectance (i.e., calculation made with a black surface) and R_p^{surf} is the surface polarized reflectance. $t_{-,+}^{*}$ is a direct transmission term where the aerosol and molecular optical thicknesses are both scaled by a factor.

[19] These factors are empirically derived and account for the neglect of the diffuse surface-atmosphere interactions. In Figure 2, we show the result of this modeling at the TOA and surface levels (dashed lines). The coefficients used to scale the molecular and aerosol optical thicknesses are respectively equal to 0.63 and 0.44. These factors are tuned here to give the best results for the particular aerosol model and load over the full range of solar zenith and azimuth angles. Although this approach is optimized here, it introduces some significant errors in the modeling of the surface contribution, resulting in errors in the TOA polarized reflectance that are as large as 0.0001 (2.5% of the signal).

[20] The simple surface model introduced in equation (8) can be easily used as the surface reflection matrix to accurately calculate the diffuse interactions between the surface and the atmosphere. We propose a slightly different approach to model the polarized reflectances measured over land by the airborne RSP that is convenient for remote sensing applications. For a given viewing geometry, we calculate the surface contribution by considering only the Fresnel reflection and we multiply this quantity by a coefficient to scale the surface to the measured one. In practice, we calculate the polarized reflectance as follows,

$$R_{p,\lambda}^{Calc} = R_{p,\lambda}^{Atm} + \left[R_{p,\lambda,Fresnel_surface}^{Atm+Surf} - R_{p,\lambda}^{Atm}\right]\xi. \tag{12}$$

[21] The dependence of the quantities on viewing geometry (μ_s, μ_v, $\varphi_s - \varphi_v$) is once again suppressed for clarity. $R_{p,\lambda Fresnel_surface}^{Atm+Surf}$ is the polarized reflectance calculated when the elements of the reflection matrix are calculated according to the Fresnel law using a surface refractive index equal to 1.5. The term in brackets corresponds to the surface contribution (see equation (9)). ξ is given by

$$\xi(\mu_s, \mu_v, \varphi_s - \varphi_v) = R_{p,2.25\mu m^{Meas}}(\mu_s, \mu_v, \varphi_s - \varphi_v)/R_p^F(\gamma), \tag{13}$$

where $R_{p,2.25}\mu m^{Meas}$ is the polarized reflectance measured at 2.25 μm.

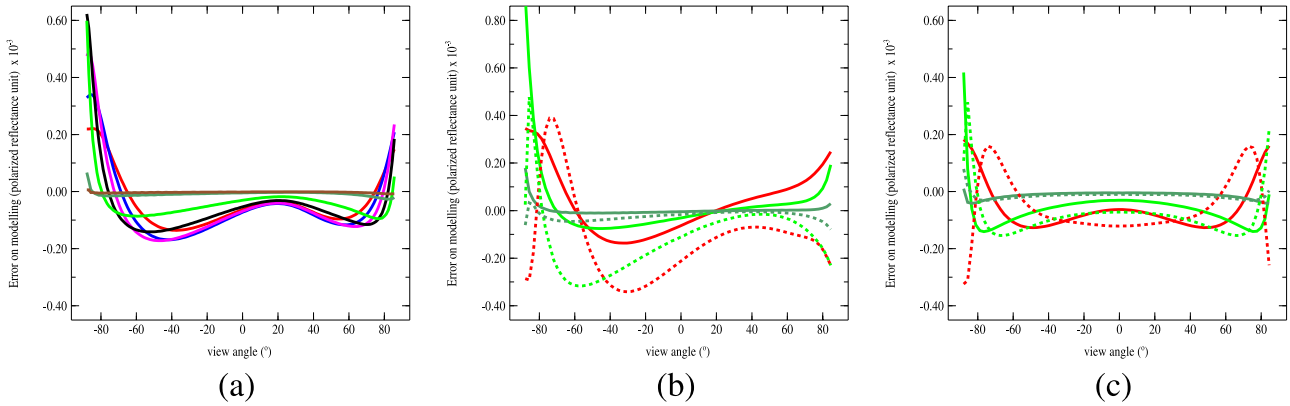

Figure 3. Errors in the modeling of the polarized reflectance shown as a function of the viewing geometry and wavelength. Calculations performed using a scaled surface reflection matrix (solid lines) or using direct transmission terms with scaling optical thicknesses (dashed lines). (a) Calculations performed in the principal plane at 0.41, 0.47, 0.55, 0.67, 0.865, 1.6, and 2.25 μm respectively in red, blue, magenta, black, green, forest, and brown. Calculations made at 0.41, 0.865, and 1.6 μm (b) 45° from the principal plane and (c) perpendicular to the principal plane. $\theta_s = 45°$, $m_r = 1.40 + 0.01i$, $r_{eff} = 0.2$ μm, $v_{eff} = 0.15$. $\tau^{0.55} = 0.1$.

[22] In equation (13), the scaling factor is derived for each view angle and allows for the fact that not all view angles see exactly the same surface as a result of aircraft attitude variations. As all the spectral polarization measurements are simultaneously acquired in each view by RSP, this modeling allows the surface contribution to be eliminated from the measurements even when different parts of the scan view different surfaces. We do note however that if a single surface type was being viewed by a remote sensing instrument, such that ξ takes a single value, or another simple parametric model of the surface can be used [*Nadal and Bréon*, 1999], then the surface model parameters should be included in the retrieval vector. The polarization generated by the Fresnel reflection (i.e., R_p^F) progressively decreases with the scattering angle and becomes null in the backscattering direction ($\Theta = 180°$). We therefore restrict this approach to scattering angles smaller than 160° in order to prevent the division by small or null values of R_p^F in equation (13).

2.3. Accuracy of the Modeling

[23] In this section, we evaluate the accuracy of our modeling of the polarized reflectances measured over land. We generate synthetic measurements using a surface polarization model representative of a vegetation canopy [*Bréon et al.*, 1995]. The surface polarized reflectance is given by

$$R_p^{Surf}(\mu_s, \mu_v, \varphi_s - \varphi_v) = \frac{1}{4(\mu_v + \mu_s)} R_p^F(\gamma), \qquad (14)$$

where R_p^F is calculated with a surface refractive index of 1.4 instead of 1.5.

[24] We compare these exact simulations to the polarized reflectances calculated following our approach using equation (12) and the one based on the use of direct transmission terms with scaling optical thicknesses (equation (11)). Pratically the model of equation (14) is used to estimate the surface polarized reflectance in equation (11) and to replace the polarized reflectance measured at 2.25 μm in equation (13). We assume here that the surface is known (i.e., well characterized using the 2.25 μm channel) in which case the errors presented in the following are directly applicable to understanding those made when modeling the actual diffuse surface-atmosphere interactions. The only caveats regarding this evaluation of the potential magnitude of modeling errors are that we are assuming that the actual surface polarization properties are not significantly more divergent from our assumed model than the simple vegetation model used here and that equation (13) is an acceptable method for dealing with surface heterogeneity. The only domain for which the modeling errors may be larger is over the scattering angle range (160–180°) that we are excluding from use. Figure 3a shows an example of the errors obtained using our modeling as a function of the viewing angles. Calculations are performed for a fine mode particle model and an aerosol optical thickness of 0.1 at 0.55 μm, in the principal plane, and for each RSP band.

[25] We observe in Figure 3a that the errors are negligible in the middle-infrared bands and increase as the wavelength decreases with the errors become critical for view angles larger than 60° where the model that we assumed and the test model are most different. The importance of the surface-atmosphere interactions mainly depends on the scattering processes that occur in the atmosphere, which increase with the optical thicknesses. This explains why the errors become larger for large view angles and roughly increase with decreasing wavelength. However, these interactions also depend on the amount of light that reaches the surface (i.e., illumination), which decreases with increasing optical thicknesses. The errors are therefore not necessarily maximal at 0.41 μm (see red line in Figure 3a) since there is a balance between the creation of errors by scattering between the surface and atmosphere and suppression of those errors by extinction.

[26] Figures 3b and 3c show a comparison between our approach (solid lines) and the one based on the use of direct

Table 1. A Priori Knowledge of the Aerosol Parameters and Associated Uncertainties

	r_g (μm)	σ	m_r	M_i
Fine mode	0.15 (0.1)	0.4 (0.1)	1.47 (0.14)	0.01 (0.015)
Coarse mode	0.8 (0.2)	0.6 (0.3)	1.53 (0.05)	0.005 (0.005)

transmission terms and scaling optical thicknesses (dashed lines) for two other viewing angle planes at 0.41, 0.865 and 1.6 μm. The scaling factors are tuned to give the best results for each viewing geometry and wavelength. For instance, the factors derived at 0.41 μm for the molecules and aerosols are respectively equal to 0.48 and 0.71, perpendicular to the principal plane, whereas these factors are equal to 0.68 and 0.81, at 45° from the principal plane. In the original parameterization, the same pair of coefficients is used independently of the wavelength and viewing geometry, which would lead to an increase in the observed errors. Our approach is in general two times more accurate and does not require tuning for different viewing geometries. We performed calculations for various viewing geometries ($-60° < \theta_v < 60°$, $0° < \varphi_s - \varphi_v < 90°$, $30° < \theta_s < 60°$) and aerosol models ($r^f_{eff} = 0.15$ μm, $v^f_{eff} = 0.17$, $r^c_{eff} = 1.97$ μm, $v^f_{eff} = 0.43$, $m = 1.47 - 0.01i$ and $0. < \tau^{0.55} < 1.5$) and found that the maximal error does not exceed 2.5×10^{-4} in any RSP band. This analysis shows that our modeling allows us to accurately simulate the diffuse atmosphere-surface interactions over a wide spectral range (0.41–2.25 μm). Based on this analysis, we now investigate the capability of the multispectral, multiangular polarized measurements of RSP to retrieve aerosol properties over land.

3. Algorithm

[27] Our retrieval approach is based on the use of an optimal estimation method. The principle of an optimal estimate is to determine the most probable atmospheric state conditional on the value of the measurements and some a priori knowledge of this medium [*Rodgers*, 2000]. The determination of the most probable atmospheric state is identical to the minimization of a cost function Φ that accounts for these different quantities:

$$\Phi = (\mathbf{Y} - \mathbf{F})^T \mathbf{C}_T^{-1} (\mathbf{Y} - \mathbf{F}) + (\mathbf{X} - \mathbf{X}_a)^T \mathbf{C}_a^{-1} (\mathbf{X} - \mathbf{X}_a), \quad (15)$$

where $\mathbf{Y}$ is the measurement vector, $\mathbf{F}$ is the simulation vector, $\mathbf{C}_T^{-1}$ is the total error covariance matrix, $\mathbf{X}$ is the atmospheric state vector, $\mathbf{X}_a$ is the a priori atmospheric state vector and $\mathbf{C}_a^{-1}$ is the a priori error covariance matrix.

[28] The first term in equation (15) corresponds to a weighted least squares error term that measures the distance between the measured polarized reflectances and the modeled polarized reflectances. We use the first six spectral bands of the RSP instrument that are in atmospheric windows: 0.41, 0.47, 0.55, 0.67, 0.87 and 1.6 μm to constrain the aerosol properties. The total error covariance matrix accounts for the measurement errors and some potential modeling errors and it is discussed in the sensitivity study in section 4.1.

[29] The second term in equation (15) is a penalty function that constrains the solution to lie near the a priori state where the "near" is quantified by the a priori error covariance matrix. The state vector X contains the aerosol parameters that allow characterizing each mode separately: N^f, r^f_g, σ^f, m^f_r, m^f_i, N^c, r^c_g, σ^c, m^c_r, m^c_i and P, the pressure level that corresponds to the height where the top of the aerosol layer is located. The a priori knowledge of the aerosol parameters is based on the aerosol climatology of *Dubovik et al.* [2002]. In Table 1, we provide the values of the *a priori* aerosol parameters (i.e., vector $\mathbf{X}_a$) and the associated uncertainties (standard deviation). The covariance matrix $\mathbf{C}_a$ is assumed diagonal where the diagonal elements correspond to the square of the standard deviation values given in Table 1. The a priori values for N^f and N^c are derived using a Look-Up-Table (LUT) approach, as explained in the following.

[30] The determination of the best solution $\mathbf{X}$ that minimizes the cost function requires the resolution of a nonlinear equation. Nonlinear systems are usually solved using the Newton-Gauss iteration procedure. In practice, the Newton Gauss procedure may not converge and need to be modified. The most widely used modification is known as the Levenberg-Marquadt method, which is implemented by the following equation:

$$\mathbf{X}^{i+1} = \mathbf{X}^i - \left[\mathbf{H}(\mathbf{X}^i) + \gamma \cdot \mathbf{I}\right]^{-1} \cdot \nabla_x \Phi(\mathbf{X}^i), \quad (16)$$

where $\mathbf{I}$ is the identity matrix with the dimensionality of the state vector, i indicates the number of iteration and γ is a positive coefficient that aids in the convergence of the iteration. $\mathbf{H}$ is known as the Hessian matrix,

$$\mathbf{H}(\mathbf{X}_i) = \nabla^2_X \Phi(\mathbf{X}_i) \approx \mathbf{C}_a^{-1} + \mathbf{K}_i^T \cdot \mathbf{C}_T^{-1} \cdot \mathbf{K}_i, \quad (17)$$

where

$$\mathbf{K}_i = \frac{\partial \mathbf{F}(\mathbf{X})}{\partial \mathbf{X}_i}. \quad (18)$$

[31] $\boldsymbol{K}$ is the Jacobian matrix, which represents the sensitivity of the forward model to the retrieved quantity (i.e., sensitivity of the polarized reflectances to the aerosol parameters).

[32] The criteria for changing the γ value is dependent on the convergence behavior. If Φ ($\mathbf{X}_{i+1}$) > Φ ($\mathbf{X}_i$) then we reject the solution $\mathbf{X}_{i+1}$ and we increase γ whereas if Φ ($\mathbf{X}_{i+1}$) < $\Phi(\mathbf{X}_i)$ then we accept the solution $\mathbf{X}_{i+1}$ and we decrease γ. For larger γ values the steepest descent dominates and the convergence is slow (i.e., small step size) but robust whereas for smaller γ values, the search turns to the faster Newtonian descent. The iteration process is stopped when there is no change of the cost function between two successive iteration steps.

[33] The optimal estimate method also provides an error diagnostic of the retrieved parameters. The Hessian matrix obtained at the final step of iteration can be used to calculate the retrieval error covariance matrix $\boldsymbol{C_x}$:

$$\mathbf{C}_x = \left(\mathbf{C}_a^{-1} + \mathbf{K}_i^T \cdot \mathbf{C}_T^{-1} \cdot \mathbf{K}_i\right)^{-1}. \quad (19)$$

The square roots of the diagonal elements of $\boldsymbol{C}_x$ allow obtaining the standard deviation associated with each retrieved parameter. The aerosol microphysical parameters

Table 2. Properties of the Fine and Coarse Modes Particles Used for the Calculations[a]

Parameters	r_g (μm)	r_{eff} (μm)	σ	v_{eff}	m_r	m_i	ω_0
Fine mode	0.1	0.149	0.4	0.175	1.44, 1.43, 1.43, 1.43, 1.425, 1.40	0.008, 0.009, 0.01, 0.011, 0.012, 0.02	0.95, 0.95, 0.93, 0.91, 0.88, 0.56
Coarse mode	0.8	1.965	0.6	0.43	1.53	0.005	0.80, 0.82, 0.84, 0.86, 0.88, 0.93

[a]The complex refractive index $m_r + im_i$ and single scattering albedo are reported at 0.41, 0.47, 0.55, 0.67, 0.87, and 1.6 μm.

contained in the vector **X** and the error retrieval covariance matrix $\boldsymbol{C_x}$ can be also used to calculate the standard deviation associated with any other aerosol parameter that depends on the elements of X. For the aerosol optical thickness, the standard deviation is given by:

$$\sigma_\tau = \sqrt{\left(\sum_{i=1}^{N}\sum_{j=1}^{N} C_{x,i,j}\frac{\partial\tau}{\partial X_i}\frac{\partial\tau}{\partial X_j}\right)}. \tag{20}$$

[34] A similar formula applies to the single scattering albedo.

[35] A first guess of the aerosol parameters ($\mathbf{X}_0$) is required to start the iterative process. A good first guess allows the number of iterations to be reduced and alleviates the problem of finding a solution **X** that is only a local minimum of the cost function Φ. We use a LUT approach in order to derive a first estimate of the aerosol optical thickness and aerosol model. The polarized reflectances are calculated for various aerosol optical thicknesses, viewing geometries and aerosol models. We consider 12 fine mode particles models (r_g^f = 0.05, 0.1, 0.15, 0.2 μm, σ^f = 0.4, m_r = 1.4, 1.47, 1.54, m_i = 0.01). We also include the coarse mode particle model described in Table 1. The polarized reflectances are calculated for aerosol optical thicknesses equal to 0, 0.05, 0.1, 0.2, 0.4, 0.8, 1 and 2 and an interpolation process is used to create a fine step. The first guess corresponds to the aerosol model and aerosol optical thickness that minimize a least squares error term calculated between the measurements and the simulations. We do not describe in details the properties of the coarse mode particles in the LUT. The reason is that the measurements investigated in the third section of this paper correspond to case studies where the small particles largely dominate the size distribution. As a first guess, the aerosol optical thickness of the coarse mode (at 0.55 μm) will be assumed to be a tenth of the total aerosol optical thickness. The properties of the aerosol models considered in the LUT allow the number density of particles associated with each mode to be derived. For retrieval with real measurements, we consider the use of the LUT to reduce the uncertainties for r_g^f and m_r^f given in Table 1 to 0.05 and 0.07, respectively, and we assume a relative uncertainty of 100% for both N^f and N^c.

[36] The residual atmospheric effect at 2.25 μm is accounted for in our retrieval process. This effect is usually small and mainly depends on the aerosol size and load [*Waquet et al.*, 2007]. We use the aerosol model retrieved with the shorter bands and a rearranged form of equation (9) to perform an atmospheric correction on the polarized reflectance measured at 2.25 μm. This correction is performed before the first iteration using the retrieved parameters obtained with the LUT approach and is refined after each iteration step.

4. Sensitivity Study

[37] The retrieval error covariance matrix defined in equation (19) can be used to simulate the retrieval errors obtained for any instrument type with synthetic measurements. In this section, we use this approach to evaluate how the different error sources and the conditions under which measurements are made affect the retrieved parameters and we discuss the sensitivity of the polarization measurements of the RSP instrument to the aerosol properties.

4.1. Aerosol Model Definition

[38] We generate synthetic measurements representative of pollutant aerosols observed over a vegetated surface. The properties of the aerosol model used for the calculations are given in Table 2. The contribution of the coarse mode to the total aerosol optical thickness is assumed to be equal to 0.1 at 0.55 μm. Calculations are made at TOA for an aerosol layer that is confined between the surface and an altitude of 3 km.

[39] We use the a priori knowledge given in Table 1 to specify the $\boldsymbol{C_a}$ matrix. We consider that the particle number density for both modes are unknown parameters ($\boldsymbol{C_a^{-1}}_{i,i} \rightarrow 0$) and that the height of the aerosol top layer is known with a relative uncertainty of 100%. We also consider that the complex refractive index of the fine mode particles may vary with the wavelength (see Table 2). The complex refractive indices of the materials of which atmospheric aerosols are typically composed show small spectral variation for the visible and near-infrared parts of the spectrum [*D'Almeida et al.*, 1991]. We therefore choose to retrieve a single complex refractive index and to constrain its spectral variation between the RSP bands assuming reasonable ranges of variation. Practically speaking, we retrieve the complex refractive index at 0.41 μm and a set of coefficients that describe its variation between the spectral bands of the RSP. Thus in this case, we use 12 fit parameters to describe the spectral behavior of the complex refractive index between 0.41 and 1.6 μm, i.e., m_r and m_i at 0.41 μm, and five coefficients for both the real and imaginary parts of the refractive index. For materials that do not have strong absorption bands in the spectral range of interest the spectral variation of both the real and the imaginary parts of the particle refractive index should not exceed 0.01 between two successive spectral bands of the RSP, except between the bands centered at 0.87 and 1.6 μm, where the large spectral range means that a maximal variability of 0.1, for the real refractive index, and 0.03 for the imaginary refractive index is realistic. These values define the a priori knowledge associated with the

Table 3. Retrieval Errors Obtained for τ^f, r_{eff}^f, m_r^f, and ω_0^f for Different Modeling of the Error Covariance Matrix[a]

Comments/Retrieval Errors	σ_τ^f	$\sigma_r_{eff}^f$ ($\times 10^{-3}$)	$\sigma_m_r^f$	$\sigma_\omega_0^f$
Reference (see section 4.1)	0.04	7.0	0.0165	0.034
(−) Errors due to calibration uncertainty	0.025	4.9	0.012	0.027
(−) Errors due to radiometric noise	0.038	7.0	0.0161	0.032
(−) Errors due to polarimetric uncertainty	0.0365	6.7	0.0157	0.031
(−) Errors due to the spectral dependence of the surface polarized reflectance	0.04	7.0	0.0165	0.034
(−) Errors of modeling	0.039	7.0	0.0165	0.0335
Considering a polarimetric accuracy of 0.005 instead of (0.001 + 0.001 × Q/I)	0.061	9.0	0.0235	0.052
Calibration errors spectrally and angularly correlated	0.025	5.1	0.0125	0.0275
Calibration errors spectrally and angularly correlated with a progressive decrease of the correlation in function of the wavelength and angle	0.07	10.0	0.032	0.052

[a](−) denotes the suppression of an error type on the calculations. The errors on τ^f, m_r^f, and ω_0^f are given at 0.55 μm. Calculations made for a total aerosol optical thickness of 0.5 at 0.55 μm ($\tau^f = 0.45$) and for $\theta_s = 45°$ and $\Delta\varphi = 45°$.

coefficients that characterize the spectral variation of the complex refractive index.

[40] A realistic estimate of inversion uncertainties must include all types of errors. The error covariance matrix accounts for measurement, as well as, modeling errors. We assume that the different sources of errors are independent in which case the total covariance matrix is given by the sum of the different error covariance matrices:

$$\mathbf{C}_T = \mathbf{C}_\varepsilon + \mathbf{C}_{cal} + \mathbf{C}_{pol} + \mathbf{C}_F. \tag{21}$$

[41] C_ε accounts for the effects of the instrumental noise, C_{cal} for radiometric calibration uncertainties and C_{pol} for any additional polarimetric accuracy uncertainties. The error covariance matrices for the RSP instrument, based on its measured signal to noise and calibration performance, are as follows:

$$\begin{aligned} C_{\varepsilon,i,j} &= \frac{10^{-7}}{\mu_s}\sqrt{R_i R_j} \\ C_{cal,i,j} &= 0.03^2 R_{p,i} R_{p,j} \\ C_{pol,i,j} &= \left(\left[0.001 + 0.001\frac{R_{p,i}}{R_i}\right]R_i\right)\left(\left[0.001 + 0.001\frac{R_{p,j}}{R_j}\right]R_j\right) \end{aligned}, \tag{22}$$

where i and j indicate the measurement number. The origin of these equations is detailed in Appendix B. The effects of having correlated measurements errors on the retrieval errors are discussed in section 4.2. For the rest of the paper, the measurement errors are assumed to be not correlated and the error covariance matrices are considered to be diagonal ($\mathbf{C}_{i,j} = 0$ for $i \neq j$). This is an assumption typically made for most evaluations of instrument and model errors on retrieval accuracies and sensitivities [e.g., *Lebsock et al.*, 2007; *Hasekamp and Landgraf*, 2007].

[42] $\mathbf{C}_F$ accounts for the effects of a change of the surface refractive index with wavelength and for the errors introduced by our modeling of the polarized reflectances (see section 2.3). $\mathbf{C}_F$ is a diagonal matrix and its elements are calculated as follows:

$$C_{F,i,i} = \left(R_{p,i}^{exact} - R_{p,i}^{calc}\right)^2 + \left(R_{p,i}^{exact} - R_{p,i}^{spec}\right)^2. \tag{23}$$

$R_{\mathrm{p},i}^{\mathrm{exact}}$ is the polarized reflectance calculated with the surface polarization model that is representative of a vegetated surface using a surface refractive index equal to 1.5. $R_{\mathrm{p},i}^{\mathrm{calc}}$ is the polarized reflectance calculated using the approximation given in equation (12). $R_{\mathrm{p},i}^{\mathrm{spec}}$ is the polarized reflectance calculated using a surface refractive index, which depends on the wavelength. According to the literature, the surface refractive index for natural matter is expected to show a spectral variation of no more than 0.03 ± 0.02 between 0.4 and 2 μm [*Pollack et al.*, 1973]. For the purpose of this sensitivity analysis, we consider a refractive index that varies linearly from 1.50 to 1.53 between 2.25 and 0.41 μm. The errors due to measurement noise depend on the total reflectance since they are dominated by detector shot noise (see equation (22)). We therefore add a Lambertian component to the simple Fresnel surface model in order to simulate a realistic level of noise in each RSP band. The spectral surface albedo is representative of a vegetated surface (deciduous) in order to be coherent with our surface polarization model.

4.2. Error Budget

[43] In Table 3, we report the retrieval errors obtained for the parameters τ^f, m_{r}^f and ω_0^f at 0.55 μm and for r_{eff}^f under different assumptions regarding the modeling of the error covariance matrix. The first row of Table 3 gives the retrieval errors obtained with the conditions detailed in section 4.1. *Mishchenko et al.* [2004] formulated the following retrieval requirements for climate research over land: 0.04 or (10%) for the aerosol optical thickness, 0.03 for the single scattering albedo, 0.1 (or 10%) for the effective radius, 0.3 (or 50%) for the effective variance, and 0.02 for the real part of the refractive index. The retrieval requirements are reached for r_{eff}^f and also for τ^f and m_{r}^f whereas the errors for ω_0^f (at 0.55 μm) are slightly larger than the requirements.

[44] In rows 2 to 5 of Table 3, we report the retrieval errors obtained when suppressing different error sources. This allows the impact of each error source on the retrieved parameters to be evaluated separately. These results show that the error budget is dominated by the measurement errors caused by calibration uncertainty. The effects of the radiative transfer modeling errors can be neglected, which is as designed: the radiative transfer model itself should never dominate retrieval errors since it can be made as accurate as necessary. This confirms that our approach for modeling the polarized reflectance (see equation (12)) is adequate for

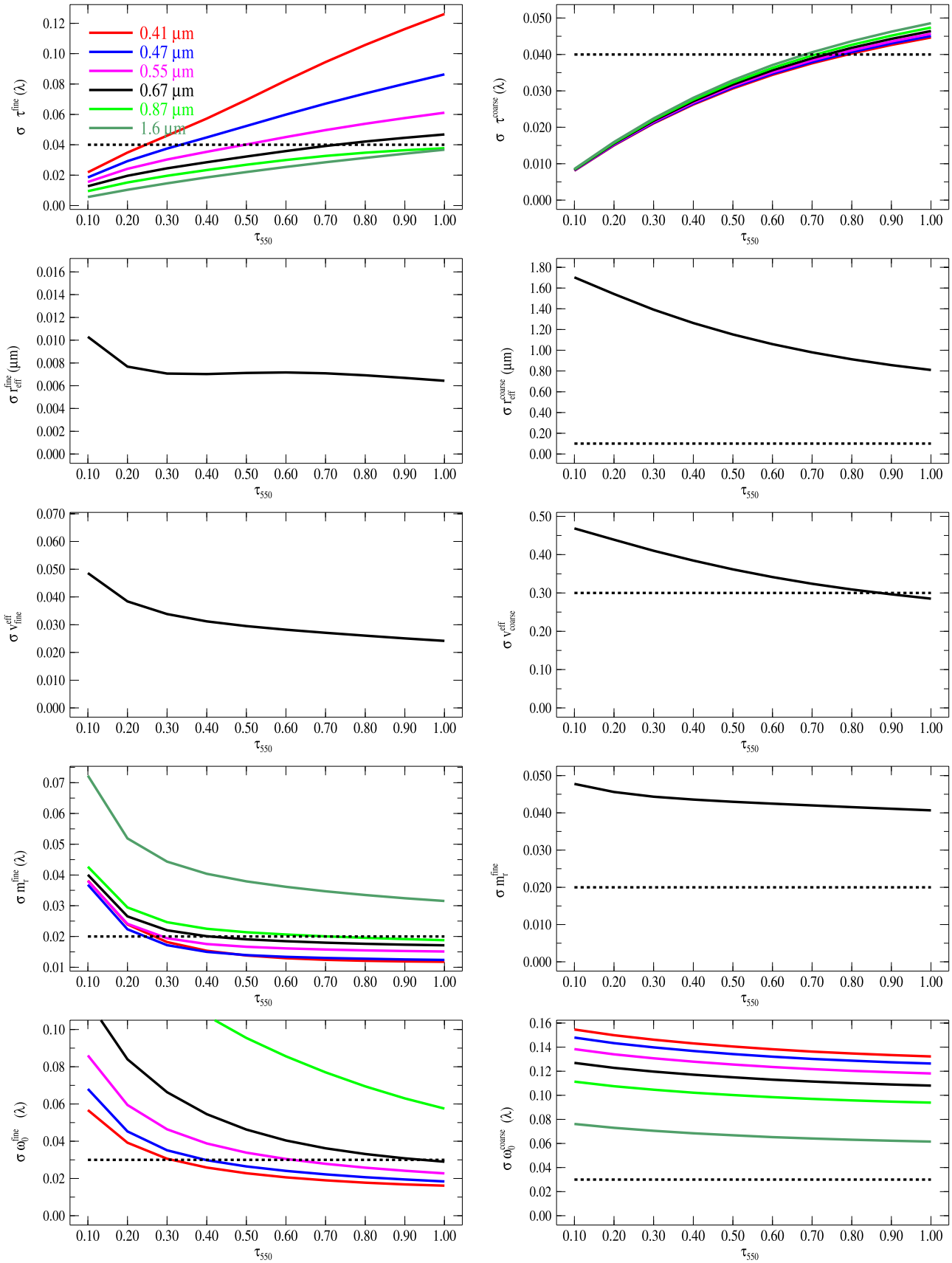
0.41 µm
0.47 µm
0.55 µm
0.67 µm
0.87 µm
1.6 µm
σ τ^fine (λ)
σ τ^coarse (λ)
σ r_eff^fine (µm)
σ r_eff^coarse (µm)
σ v_fine^eff
σ v_coarse^eff
σ m_r^fine (λ)
σ m_r^fine
σ ω_0^fine (λ)
σ ω_0^coarse (λ)
τ_550

Figure 4

highly accurate measurements with a broad spectral baseline. It also indicates that the effects of a realistic nongray surface polarization do not affect the retrieved parameters, at least for an AOT larger than 0.5 at 0.55 μm. The polarimetric accuracy for the RSP instrument is expected to be better than 0.002 (see equation (22)). When considering a larger error for the polarization ratio of 0.005, we observe a significant increase in the errors and the retrieval requirements are not reached for most aerosol parameters. This result confirms that a high polarimetric accuracy is required in order to derive the aerosol parameters with the level of accuracy suggested by *Mishchenko et al.* [2004].

[45] We also examined the effect of having errors due to calibration uncertainty that are correlated. This is implemented by introducing off-diagonal elements into the calibration covariance matrix that is defined in equation (22). The first case corresponds to measurement errors caused by calibration accuracy that are spectrally and angularly completely correlated as might be the case with a sensor such as the RSP that scans the fields of view of one set of detectors and that uses a pristine white reflector for its radiometric calibration. As shown in Table 3, in this case the errors in the retrieval of the aerosol parameters are significantly smaller than is the case for independent error sources. We also consider the case where the correlation progressively decreases with the wavelength and difference in the view angle. The results show that for a sensor where this is the case the errors in the retrieval of the aerosol parameters are substantially larger than for the base case. This result confirms the findings of *Hasekamp and Landgraf* [2007], in which a similar tendency was observed. In the following, we use a diagonal error covariance matrix since the results are intermediate between a completely correlated error matrix and one where correlations degrade with spectral and angular distance. It also makes our results more easily comparable with those of previous investigators who invariably use diagonal error covariance matrices.

4.3. Impact of the Particle Load and Size on the Error Budget

[46] The retrieval errors obtained for $\tau(\lambda)$, r_{eff}, v_{eff}, $m_r(\lambda)$, $m_i(\lambda)$, $\omega_0(\lambda)$ of each mode, are shown in Figure 4 as a function of the total aerosol optical thickness at 0.55 μm. The errors associated with the aerosol parameters generally decrease with aerosol optical thickness (AOT), except for the AOT itself. The contribution of the light scattered by the aerosol to the up-welling polarized light increases with the AOT, which therefore leads to an increase of the sensitivity of our algorithm to the aerosol properties. The increase of the errors associated with the AOT is explained by the fact that the errors in N increase with N (not shown) and because the AOT is closely connected to this parameter (see equation (4)). The relative errors in the fine mode AOT however decrease for increasing AOT and remain under the required value for all the wavelengths considered here ($\sigma_\tau(\lambda)/\tau^{\mathrm{f}}(\lambda) < 10\%$). For the fine mode particles, the requirements for r_{eff} and v_{eff} are met for any AOT values larger than 0.1 at 0.55 μm, whereas for m_{r} and ω_0, the requirements are only reached in three spectral bands (0.41, 0.47, 0.55 μm) and for AOT respectively larger than 0.3 and 0.6. For the coarse mode particles, we do not reach the required accuracy for most of the parameters here. This is because the contribution of the coarse mode to the total AOT is small in this test case ($\tau_{\mathrm{c}}^{0.55}/\tau^{0.55} = 0.1$).

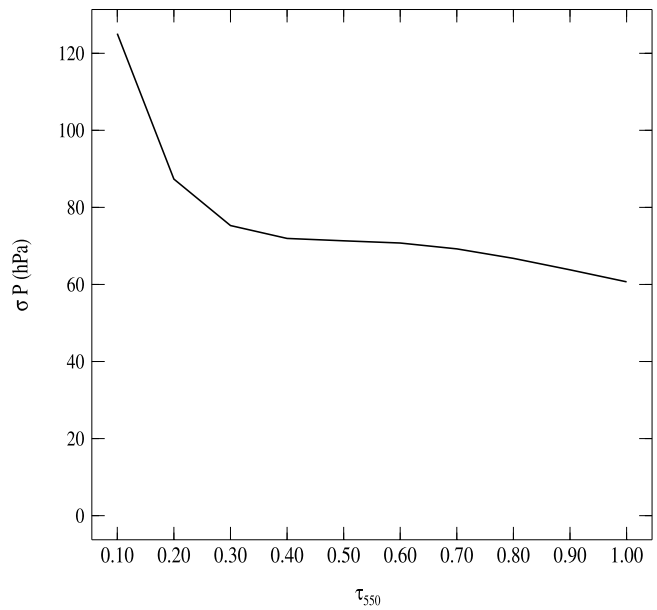

Figure 5. Retrieval errors for pressure level of top of aerosol layer, P, as a function of the total aerosol optical thickness at 0.55 μm.

[47] Figure 5 shows that there is also useful information about the height of the top of the aerosol layer. The error in the pressure level of the top of the aerosol layer is less than 70 hPa for AOT greater than 0.6 at 0.55 μm when the true mixed layer depth is P = 700 hPa. This corresponds to an error of 0.8 km when the aerosol altitude is 3 km. It is important to note that we are primarily interested in retrieving P to ensure that large retrieval and/or fitting errors do not occur in the presence of thick aerosol layers such as smoke plumes and that erroneous assumptions about P do not therefore cause a bias in our retrievals.

[48] The sensitivity of our algorithm to the properties of small particles also varies as a function of their size. Figure 6 shows the retrieval errors obtained for m_{r}^f at 0.55 μm and r_{eff}^f as a function of the effective radius. The range of effective radius shown in Figure 6 covers the expected range of size for the fine mode (0.1–0.6 μm). We observe that the retrieval errors for the real part of the refractive index and effective radius respectively decrease and increase with the effective radius. Figure 6 indicates that the retrieval errors for r_{eff}^f remains within the required value for any small particles that belong to the fine mode. It also indicates that the

Figure 4. Retrieval errors for the fine mode parameters τ^f, r_{eff}^f, v_{eff}^f, m_r^f, ω_0^f (right) and for the coarse mode parameters τ^c, r_{eff}^c, $v_{eff}v_{eff}^c$, m_r^c, ω_0^c (left). The dashed lines correspond to the accuracy requirements suggested by *Mishchenko et al.* [2004]. The aerosol optical thicknesses associated with each mode can be calculated using the following formulae: $\tau^{\mathrm{c}} = 0.1\tau$ and $\tau^{\mathrm{f}} = \tau - \tau^{\mathrm{c}}$. The properties of the aerosol models used in the calculations are given in Table 3. Computations are performed at TOA for $\theta_{\mathrm{s}} = 45°$ and $\Delta\varphi = 45°$.

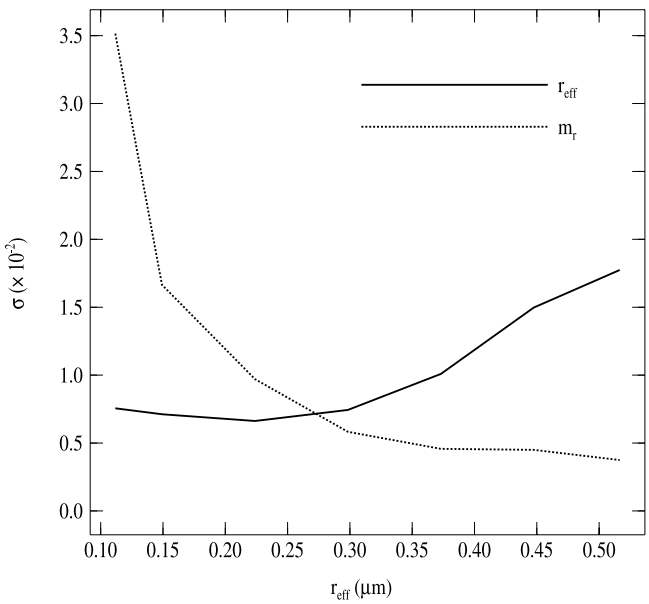

Figure 6. Retrieval errors for r_{eff}^f and m_r^f at 0.55 μm as a function of the effective radius. Calculations were made for an aerosol optical thickness equal of 0.5 at 0.55 μm and $\Delta\varphi$ = 45°, θ_s = 45°. The aerosols properties used for the calculations are given in Table 3. The sampling of effective radius uses geometric mean radii, r_g, of 0.075, 0.1, 0.15, 0.20, 0.25, 0.30 and 0.35 with an effective variance of 0.2.

sensitivity of our algorithm to m_r is largest for the largest particles of the fine mode. The reason for this is that when particles are small compared with the measurement wavelength they act like Rayleigh scatterers [*Hansen and Travis*, 1974; *Mishchenko et al.*, 2002], and any sensitivity to the refractive index is lost. It is therefore crucial, in order to have sensitivity to the refractive index of fine mode particles, to have measurements at short wavelengths as we describe in the following section.

4.4. Dependence of the Error Budget on the Spectral Range and Viewing Geometry

[49] A retrieval error analysis in which the two bands in the blue part of the spectrum are removed (0.41 and 0.47 μm) gives errors of 0.04 for ω_0^f (at 0.55 μm), 0.011 μm for r_{eff}^f, 0.03 for m_r^f (at 0.55 μm) and 140 hPa for *P*. When using the full spectral range of the RSP, we found errors equal to 0.023 for ω_0^f (at 0.41 μm), 0.007 μm for r_{eff}^f, 0.014 for m_r^f (at 0.41 μm) and 70 for *P* (calculations made for θ_s = 45°, $\Delta\varphi$ = 45° and AOT = 0.5 at 0.55 μm, see section 4.1 for other conditions). For the viewing geometry and the atmospheric model considered here, these calculations show that polarized spectral bands shorter than 0.5 μm allow the aerosol top layer height to be estimated together with retrieving ω_0^f and m_r^f within the requirements given by *Mishchenko et al.* [2004]. Polarization measurements in the visible and near-infrared part of the spectrum (0.55 < λ < 1.6 μm) only allow the robust retrieval of r_{eff}^f and AOT. *Lebsock et al.* [2007] reached similar conclusions although their fine mode particles were large enough that they found sensitivity to refractive index in their analysis of the two POLDER bands at 0.673 and 0.861 μm.

[50] Figure 7 shows the retrieval errors obtained for τ^f and ω_0^f for different viewing geometry as a function of the AOT at 0.55 μm. Calculations are made for different values of relative azimuth angle and solar zenith angle. Figure 7 demonstrates that the errors in the AOT are significantly larger for a relative azimuth angle of 90° than for 45°. Similar behavior is observed for the other aerosol parameters. The errors for r_{eff}^f, v_{eff}^f and m_r^f at 0.41 μm respectively reach 0.012, 0.05 and 0.035 for an AOT of 0.5 at 0.55 μm. The reason is that the measurements performed in the case of a relative azimuth angle of 45° sample a larger range of scattering angle than in the case of a relative azimuth angle of 90°. The solar zenith angle also affects the errors in the retrieval of aerosol parameters. The retrieval errors for an AOT equal to 0.5 are equal to 0.041, 0.040 and 0.053, respectively for θ_s equal to 30, 45 and 60°. The errors on ω_0^f are also dependent on the relative azimuth angle and on the solar zenith angle as shown in Figure 7. However, it is the magnitude of the AOT that dominates the accuracy of the retrieval of ω_0^f primarily because neither remote sensing retrievals, nor the radiation budget of the Earth are really sensitive to the single-scattering albedo *per se*. Rather, the absorption optical depth is the absorption parameter that passive remote sensing is sensitive to and is also what determines whether solar radiation is absorbed in the atmosphere of the Earth. Additional calculations made with

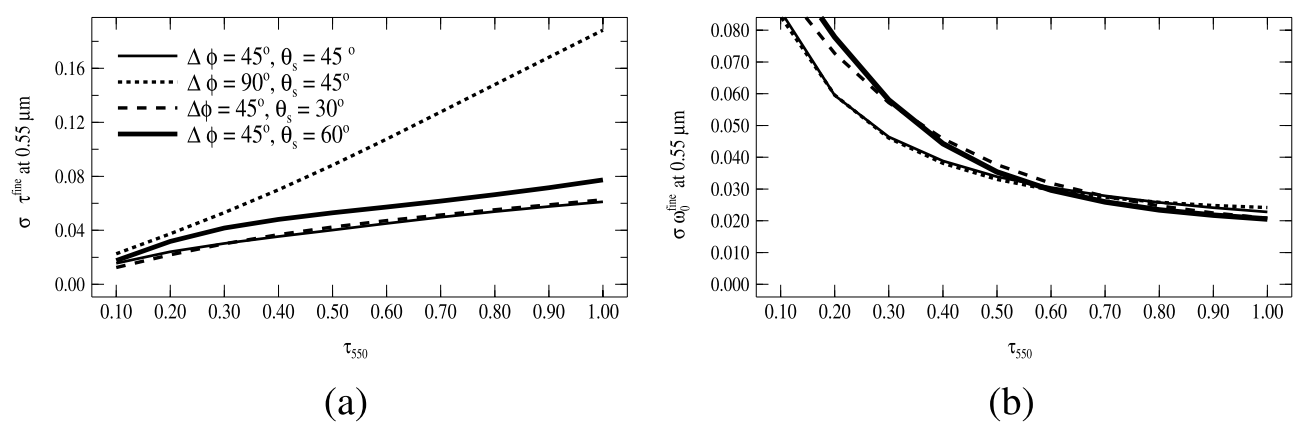

Figure 7. Retrieval errors for τ^f and ω_0^f at 0.55 μm as a function of the aerosol optical thickness at 0.55 μm for $\Delta\varphi$ = 45°, θ_s = 45° (solid lines), $\Delta\varphi$ = 90°, θ_s = 45° (dots), and $\Delta\varphi$ = 45°, θ_s = 30° (solid lines).

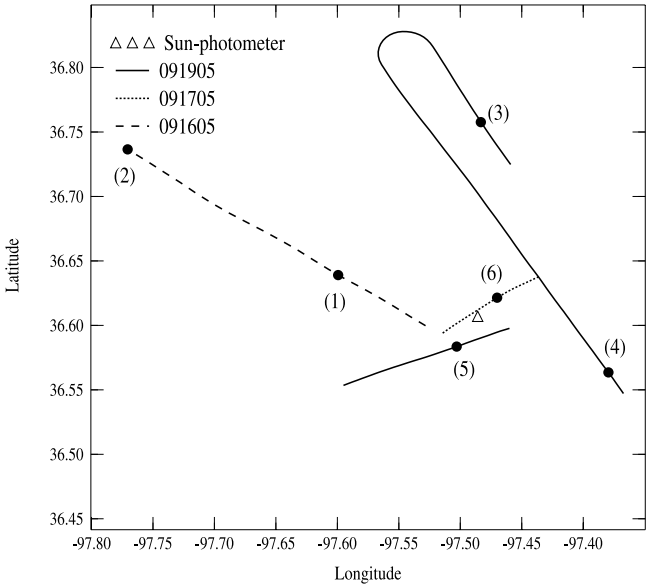

Figure 8. Selection of flight track segments performed during the ALIVE experiment. The triangle indicates the position of the AERONET Sun photometer. The dots and associated numbers indicate the location of scans of measurements shown in Figure 10.

various relative solar azimuth angle values show that all the parameters of the fine mode can be retrieved with the required accuracies (at least in 3 spectral bands for the spectral quantities), for $\Delta\varphi$ varying between 0 and 65° and between 125 and 180° (calculations made for θ_s = 45°). For relative azimuth angles between 65 and 125° prior assumptions about the real part of the refractive index will become important for the accuracy of the retrievals.

5. Application to Field Experiments

[51] In this section, we analyze the data taken by the RSP instrument during the Aerosol Lidar Validation Experiment (ALIVE) in Oklahoma and during a flight performed over a thick smoke plume above the Mojave desert of Southern California.

5.1. The ALIVE Experiment

[52] The ALIVE experiment took place over the Department of Energy Atmospheric Radiation Measurements (ARM; [*Ackerman and Stokes* 2003]) program facility in the Southern Great Plains (SGP). The primary purpose of this campaign was to collect airborne remote sensing data of atmospheric aerosols in order to perform a validation study of the SGP ground-based lidars. The RSP instrument participated in this campaign aboard the Sky Research Inc. Jet stream-31 (J31) research aircraft and acquired good quality data throughout all twelve flights performed between 12 and 22 September 2005. During this campaign, the RSP instrument flew on the J31 in collaboration with the NASA Ames Airborne Tracking 14-Channel Sun photometer (AATS-14). The AATS-14 instrument, mounted on the top of the aircraft, tracks the direct solar beam and measures its attenuation in fourteen spectral channels. These measurements allowed the aerosol optical thickness of the column above the aircraft to be derived in 13 bands between 0.353 and 2.105 μm [*Russell et al.*, 1999; *Schmid et al.*, 1997, 2003].

[53] All the flights were organized around the SGP ARM Cloud central facility (N36°36′25″, W97°29′09″), which is equipped with a Cimel Sun photometer that is part of the federated Aerosol Robotic Network (AERONET). The operational inversion algorithm developed for the analysis of the AERONET Sun photometer measurements provides the spectral aerosol optical thickness, the aerosol complex refractive index and the particle size distribution between 0.05 and 15 μm [*Dubovik and King*, 2000]. Figure 8 shows examples of flight track segments performed during this campaign. In Table 4, we report the main characteristics of the flights performed during the ALIVE experiment. Table 4 shows that all the flights were performed with low aerosol loading ($\tau < 0.165$ at 0.5 μm) and were often perturbed by the occurrence of cirrus. A cloud-screening algorithm has been developed for the analysis of the AATS measurements and allowed us to select scenes for which the direct beam of the sun was cloud free. Vertical profiles of the aerosol properties and columnar water vapor were also derived with the AATS-14 instrument during spiral descents and ascents of the Jet stream-31. Figure 9 shows examples of vertical profiles of the aerosol optical thickness measured by the AATS-14

Table 4. Characteristics of the Flights Performed During the ALIVE Experiment[a]

Date	Time (UT)	Mean Altitude or Min and Max Values (km)	τ^f	τ^c	Comments
09/11/05	–	–	–	–	technical flight
09/12/05	–	–	–	–	cloudy condition
09/13/05	1730–1845	0.5–5.5	–	–	no AERONET data available, very clear condition (observed by the AATS-14)
09/16/05	1545–1645	0.5–5.5	0.075	0.000	2 flights, clear condition
09/17/05	2130–2320	1.5–5.5	0.13	0.035	few cirrus
09/19/05	1415–1615	0.5–7.5	0.01	0.055	2 flights, few cirrus
	1730–2000	0.5–7.0			
09/20/05	1530–1715	0.5–5.5	0.135	0.040	2 flights, many cirrus
	2030–2045	0.5–4.5			(first flight only)
09/21/05	1500–1540	0.5–5.5	0.115	0.035	2 flights, few Cirrus
	1700–1900	0.5–7.0			
09/22/05	1430–1730	0.5–4.0	0.114	0.035	2 flights, few Cirrus
	1830–2200	4.0			

[a]The aerosol optical thickness for the fine and coarse modes are given at 0.5 μm and were derived from AERONET observations (daily average).

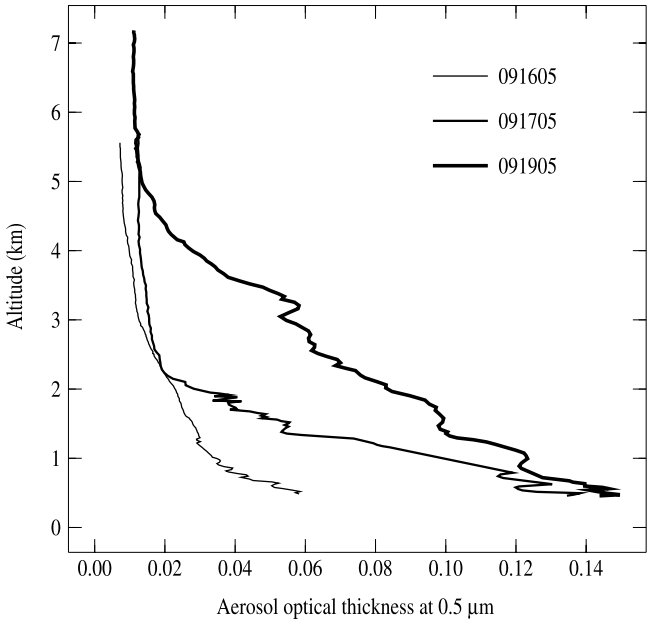

Figure 9. Vertical profile of the AOT measured by the AATS instrument at 0.5 μm.

instrument. The measured profiles show that the particles were located primarily in the first 2 to 3 km of the atmosphere. In the following, we focus on the analysis of the measurements performed on the 16, 17, and 19 September since the observed surfaces and particles were representative of the ones usually observed during the ALIVE campaign.

[54] Figure 10 shows some scans of polarized reflectance measured by the RSP as a function of the view angle. The RSP measurements are corrected for gaseous absorption using a parameterization that has a two-pass transmission correction above the aircraft level and uses an effective absorption optical depth in the calculation of upwelling polarized radiances below the aircraft. The relevant parameters were estimated using correlated *k*-distributions [*Lacis and Oinas*, 1991] with 1-nm widths that were integrated over the RSP spectral band responses. The form of the parameterization is motivated by the fact that the centers of the methane and carbon dioxide absorption lines that affect the 1.6 and 2.25 μm bands are saturated high in the atmosphere, such that it is only weaker absorption in line wings that affects the transfer of radiation through aerosol layers in the lower atmosphere. Water vapor continuum absorption is also relevant to the simulation of scattering in the lower atmosphere and is included in the parameterization of the effective absorption optical depth. The amount of column water vapor present is prescribed using AERONET or AATS-14 measurements. The majority of ozone is so high in the atmosphere that it can be accounted for using a simple transmission correction to the direct beam of the sun, with the ozone column amount being prescribed using the estimates provided by TOMS, or the Ozone Monitoring Instrument (OMI). In the retrieval process, we only include the errors in the measurements described in equation (22). For the measurements performed during the ALIVE campaign, we conservatively estimate an absolute radiometric calibration uncertainty equal to 6% for the bands centered at 0.41, 0.47, 0.55 and 0.67 μm and 3% for the others (see Appendix C for source of calibration). The viewing geometries that correspond to scattering angles larger than 160° are not considered in the retrieval process and are therefore not shown (see section 2).

[55] During the ALIVE campaign, we observed heterogeneous scenes consisting of vegetated surfaces and bare soil. Different parts of the scan therefore view different surface types that are associated with different magnitudes of the surface polarization, which explains the strong fluctuations that are observed in the measured polarized reflectances. It is important to note that the fluctuations in all the spectral bands are strongly correlated. The differences in the polarization magnitude from one scan to another can be explained by a change in the observed surfaces (e.g., scans (a) and (b)) or by a change in the viewing geometry (e.g., scans (c) and (d)). The scans were performed in different planes of observation, which provided measurements with different ranges of scattering angle (see Table 5). The angular and spectral behavior is consistent with our hypotheses regarding the surface polarization properties. The spectral behavior of the observed polarized reflectance is similar to that of atmospheric scattering, which is consistent with our hypothesis that the surface polarization does not show much spectral dependence. The polarized reflectance decreases with the scattering angle, which is consistent with all the extant observations in the literature that have shown that the Fresnel law is the primary determinant of the surface polarization over land.

[56] In Figure 10, we show the polarized reflectance simulated at the aircraft altitude. We observe that the use of the 2.25 μm measurement allows the effects of the various surface types to be compensated efficiently. For scans (a) and (b), we report the results obtained with the LUT approach, since the latter is sufficient to obtain a fit of the measurements within the expected uncertainties. For the others cases, we use the whole retrieval process including the parameters N^f, r_g^f, σ^f and m_r^f. We do not try to retrieve the absorption and the altitude of the aerosol since the sensitivity to these parameters is weak at such low AOT. Figure 10 shows that the assumptions made allow good fits to be obtained for each set of measurements. The maximal error in the modeling of the polarized reflectance is equal to 4×10^{-3} and is observed at the maximal polarization level for the observations performed under very clear conditions (see Figure 10b). For the others cases associated with

Figure 10. Polarized reflectance measured at the aircraft level (solid lines) and simulated polarized reflectance (dashed lines) as a function of the viewing angle. The wavelengths of the data and simulations are 0.41, 0.47, 0.55, 0.67, 0.865, and 1.6 μm respectively in blue, magenta, black, green, dark green, and brown. The differences between the simulated and measured polarized reflectances are shown at the top of the figures. Scans (a) and (b) performed on 16 September 2005, scans (c), (d) and (e) performed on 19 September 2005, and scan (f) performed on 17 September 2005. See Table 5 for associated viewing geometry and atmospheric conditions and Figure 8 for the location.

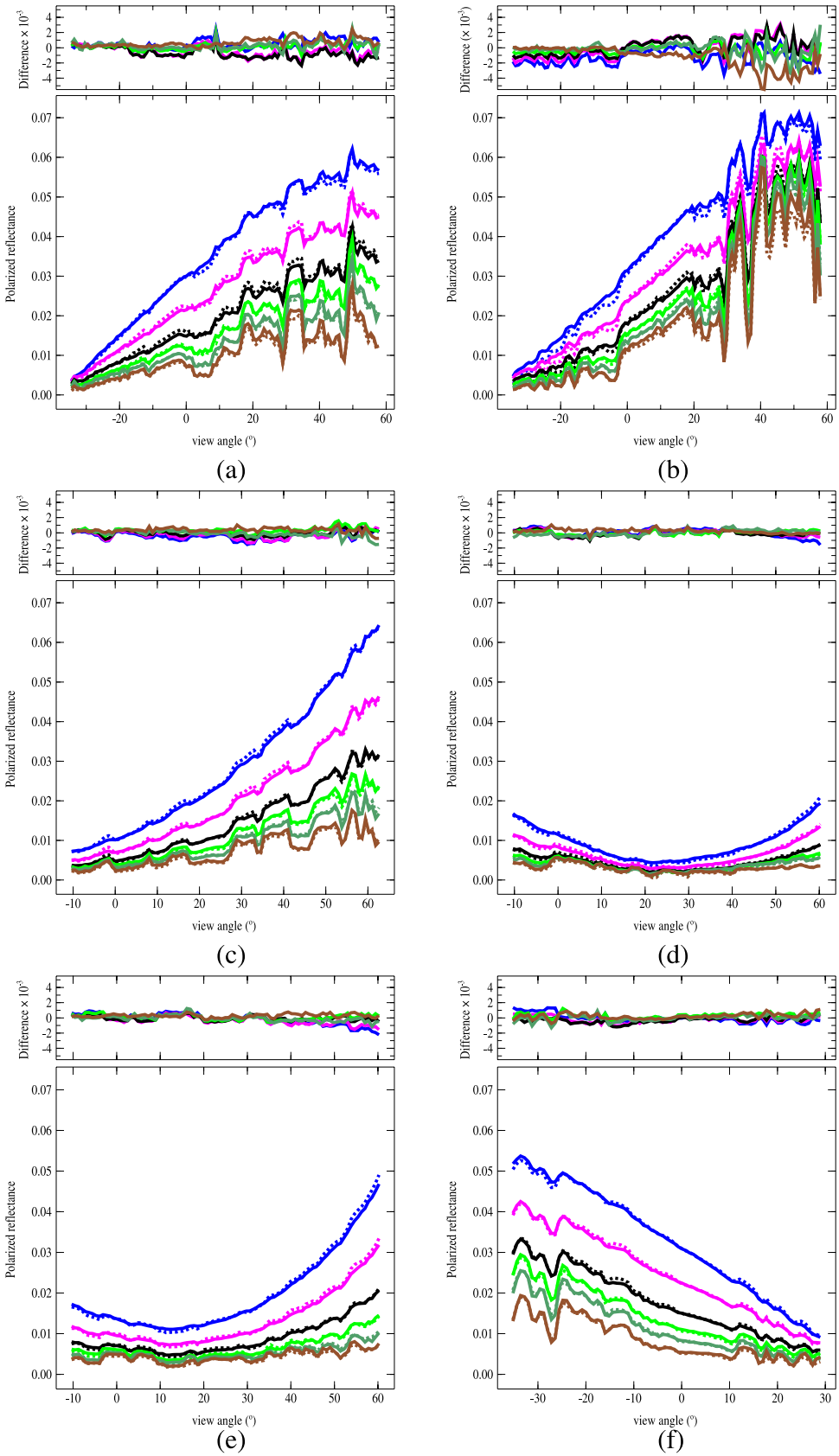

Figure 10

Table 5. Viewing Geometries Associated With the RSP Scans in Figure 10[a]

	Viewing Geometry			RSP Retrievals			AERONET Retrievals			
Scan	Θ	θ_s	φ_r	τ (0.67 μm)	r_{eff}	m_r	τ^f (0.675 μm)	τ^c (0.675 μm)	r^f_{eff}	m_r (0.675 μm)
a	70–160	56	−186	0.045	–	–	0.03	0.013	0.14	1.46
b	70–160	56	−186	0.04	–	–				
c	90–150	36	−130	0.085 (0.005)	0.175 (0.005)	1.50 (0.01)	0.08	0.05	0.165	1.48
d	135–160	36.5	37	0.09 (0.01)	0.19 (0.005)	1.475 (0.02)				
e	125–145	35	−67	0.07 (0.005)	0.18 (0.01)	1.475 (0.015)				
f	85–150	59	6	0.095 (0.005)	0.19 (0.005)	1.42 (0.01)	0.075	0.025	0.165	1.35

[a]The aerosol parameters were retrieved from the RSP and AERONET measurements. Aircraft and ground-based measurements performed within 15 minutes. The values in brackets correspond to the standard deviation associated with the retrieved parameters.

slightly larger AOTs, the maximal errors on the modeling of the polarized reflectance do not exceed 2×10^{-3}. In Table 5, together with the viewing geometry associated with each scan, we report the aerosol parameters retrieved with the RSP measurements and the coincident AERONET retrievals. These results show that our approach allows the AOT of the fine mode particles to be retrieved with a maximal error of 0.02 at 0.67 μm. The effective radius is retrieved with a maximum error of 0.025 μm, which indicates that the spectral dependence of the fine mode AOT is also well retrieved. The agreement between the retrieved refractive indices is good for 19 September 2005 with a bias of 0.003 and standard deviation of 0.014, but on 17 September 2005 the retrieval using RSP data is 1.42 while the retrieval using Cimel data is 1.35. The fact that the Cimel estimates of AOT are also biased low against the polarimetric retrievals by 0.02 suggests that the Cimel refractive index estimates may be the source of the discrepancy [*Dubovik and King*, 2000, Figure 4]. This is particularly likely given that the relative humidity at that time was only 55%, which is far too low to strongly hydrate small particles to a level where a refractive index of 1.35 is reasonable.

[57] The uncertainty in the refractive index retrieved with our algorithm is lower than that we presented in our sensitivity study analysis for the same AOT (see Figure 4). This is because the sensitivity of the polarization measurements to aerosol properties is slightly larger for the case of aircraft observations than for the case of observations from space. The inclusion of the coarse mode particles in the inversion slightly affects the retrievals obtained for the fine mode and the retrieval error budget. For instance, when including the coarse mode parameters (i.e., N^c, r^c_g, σ^c and m^c_r) in the inversion, we found for scan (e): $\tau^f_{0.67} = 0.095$ (0.01), $r^f_{eff} = 0.18$ (0.01) μm, $m^f_r = 1.47$ (0.02), $\tau^c_{0.67} = 3.6 \times 10^{-4}$ (3.2×10^{-4}), $r^c_{eff} = 1.97$ (1.85) μm and $m^c_r = 1.53$ (0.05); for scan (f), we found: $\tau^f_{0.67} = 0.065$ (0.005), $r^f_{eff} = 0.17$ (0.005) μm, $m^f_r = 1.47$ (0.02), $\tau^c_{0.67} = 1 \times 10^{-4}$ (0.8×10^{-4}), $r^c_{eff} = 1.935$ (1.8) μm and $m^c_r = 1.535$ (0.05). We found maximal changes of 0.025 for the fine mode AOT, 0.02 μm for the fine mode effective radius and 0.05 for the fine mode real refractive index. The fitting accuracy is slightly reduced when considering the coarse mode particles in the inversion, i.e., error term of 0.27×10^{-6} instead of 0.25×10^{-6}, for scan (e) and error term of 0.25×10^{-6} instead of 0.2×10^{-6} for scan (f). The retrieved coarse mode AOTs are extremely small and associated with large standard deviation values. The other characteristics of the coarse mode particles (size and refractive index) are therefore not accurately retrieved. These results indicate that there is little sensitivity of our approach to the coarse mode particles at least for coarse mode AOTs less than 0.05 with a very large coarse particle mode. For such low AOT, the effects of the coarse particles on the fine mode retrievals can be considered as a nuisance parameter and should be included in the total error covariance matrix.

5.2. Smoke Measurements

[58] Several massive wildfires were raging across Southern California in late October 2003, burning more than 300,000 hectares of biome [*Keeley*, 2004] and affecting the atmospheric chemistry and air quality [*Mühle et al.*, 2007]. On 29 October 2003, the RSP instrument, installed on a small survey plane (Cessna 310), flew over some fires in the Simi Valley and over the Mojave Desert to where a significant amount of smoke had been transported. Biomass burning particles are usually characterized by large absorption properties and a size distribution dominated by the fine mode [*Dubovik et al.*, 2002]. These particles are usually injected into the atmosphere at high altitudes and can be transported [*Hsu et al.*, 2004] over long distances [*Hoff et al.*, 2005, *Hlavka et al.*, 2005]. These characteristics have

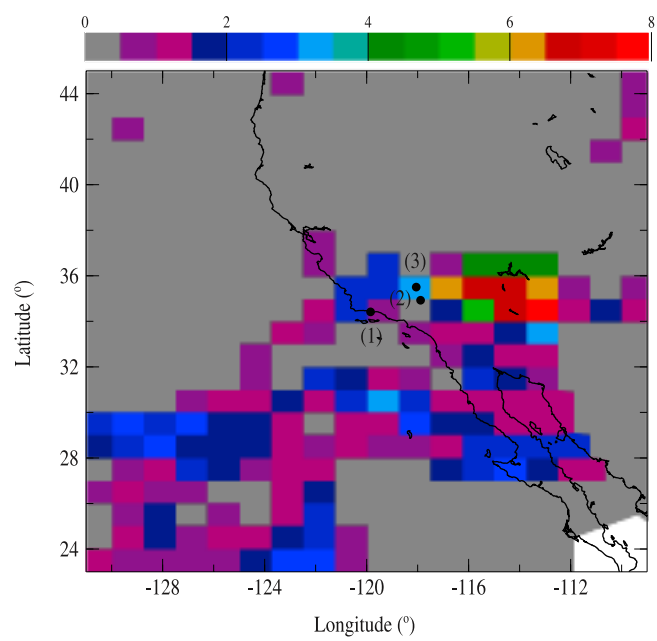

Figure 11. Aerosol index TOMS daily image for 29 October 2003. Dots: (1) and (2) locations of the AERONET Sun photometers based at the UCSB and Rogers Dry Lake stations; (3) location of the RSP scan shown in Figure 14.

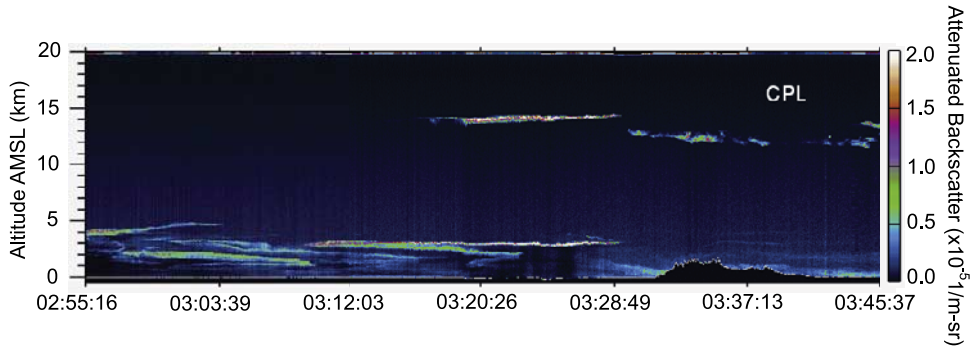

Figure 12. Backscattering lidar coefficient profiles measured at 0.532 μm by the CPL instrument shown as a function of acquisition time. Measurements performed on 28 October 2003.

been confirmed from space-based and ground-based observations. In Figure 11, we show the Aerosol Index derived from the TOMS Earth Probe observations. We observe that the smoke plume was extended over the south of the USA and Mexico and was being transported west. Values as large as 8 can be observed, which is indicative of the presence of a large amount of absorbing particles in the air at high altitude [*Herman et al.*, 1997]. The aerosol load was highly variable on 29 October 2003 and there was some patchy cirrus cloud cover present. The Sun photometer located on the west coast at the University of California at Santa Barbara station (N 34°24′54″, W 119°50′42″) performed measurements for clear-sky conditions just after the end of the flight. The AOTs of the fine and coarse mode were 1.385 and 0.039 respectively at a reference wavelength of 0.5 μm. This observation confirms that the absorbing aerosols observed by TOMS mainly belonged to the fine mode. Some information about the vertical extent of the smoke plumes was also available. The NASA Goddard Space Flight Center (GSFC) Cloud Physics Lidar (CPL) obtained measurements from the NASA ER-2 aircraft over southern California the day prior to the RSP flight. In Figure 12, we show the backscattering lidar coefficient measured at 0.532 μm by the CPL instrument. These measurements show aerosol layers detached from the ground that are located between 1 and 5 km as well as some thin cirrus on the second part of the flight track.

[59] In the following, we investigate measurements performed during the over-flight of the Mojave Desert. During this part of the flight observers on the plane noted that there was minimal cirrus cloud cover overhead and that the top of the aerosol layer was close to the aircraft level. In order to study the effects of the aerosol vertical distribution on the polarization measurements, we considered different atmospheric structures in the LUT calculations. We calculated the polarized reflectance contained in the LUT under the assumption that the particles were located between the surface and three different aerosol layer top heights equal to 2.4, 3.6 and 4.8 km. These values are chosen based on the aircraft and surface altitudes (4.8 and 1.2 km respectively) and allow us to break the aerosol into three layers each of 1.2 km thickness. We also consider the case where the aerosol layer may be detached from the ground and allowed the aerosol layer to be located between 2.4 and 3.6 km, 2.4 and 4.8 km, or 3.6 and 4.8 km. We show in Figure 13 the polarized reflectance measured at 0.41, 0.47 and 0.55 μm and the polarized reflectance calculated for different atmospheric profiles. The calculations are made for the aerosol model that is retrieved for the case in which the particles are located between the 3.6 and 4.8 km.

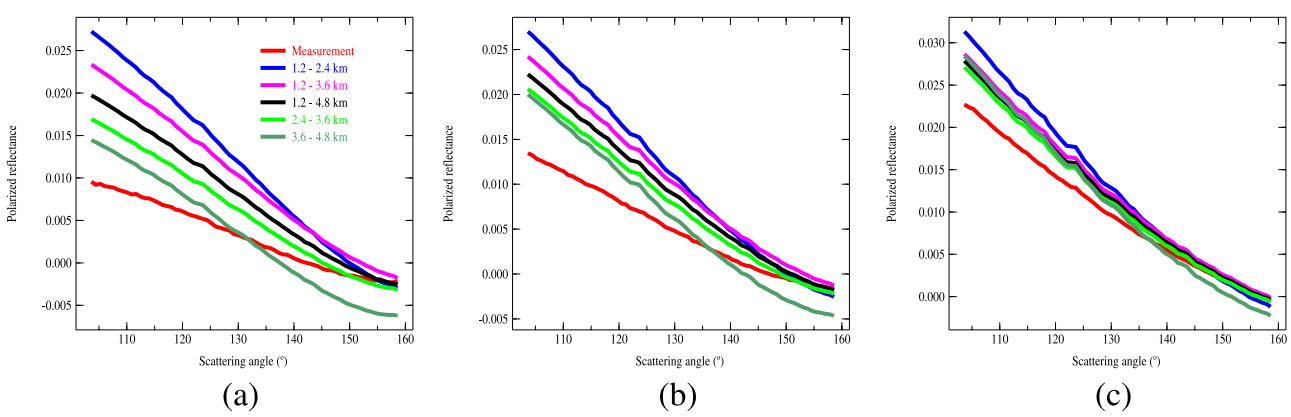

Figure 13. Polarized reflectance at (a) 0.41, (b) 0.47, (c) 0.55 μm as a function of the scattering angle. Measurements (red lines) and simulations calculated for different atmospheric profiles: aerosols between the surface and 2.4 km (blue), 3.6 km (magenta), 4.8 km (black), between 2.4 and 4.8 km (green) and between 3.6 and 4.8 km (dark green). Calculations made for an AOT of 0.57 at 0.67 μm and the aerosol model used for the LUT calculations (m_L = 1.54 − 0.01i, r_g = 0.1 μm, σ = 0.4).

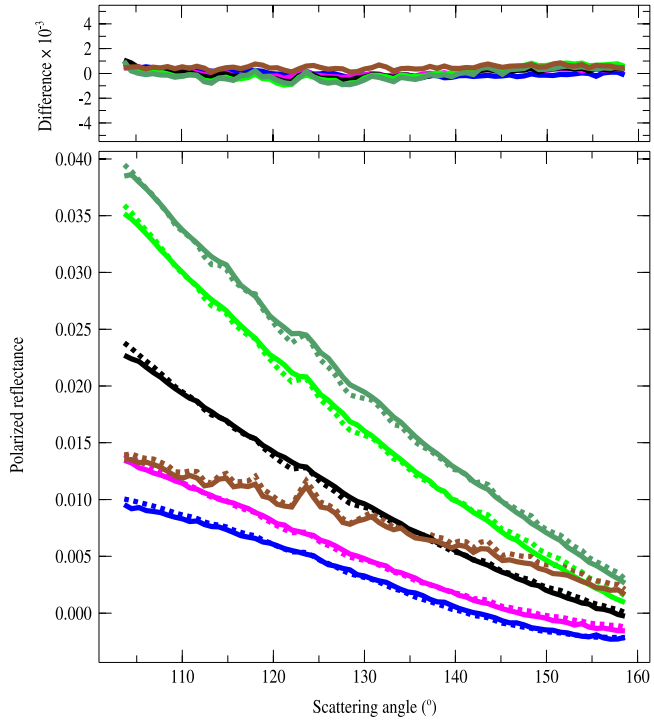

Figure 14. Scan of polarized reflectance measured by the RSP instrument over the smoke plume as a function of the scattering angle. The wavelengths are 0.41, 0.47, 0.55, 0.67, 0.87, and 1.6 μm and are shown respectively as blue, magenta, black, green, dark green, and brown. The differences between the measured (solid lines) and simulated (dashed lines) polarized reflectances are shown on top. The measurements were acquired in the principal plane with a solar zenith angle of 50°.

[60] We observe that the effects of the aerosol vertical distribution on the polarization measurements decrease with the wavelength, as expected. The simulations performed at 0.41 and 0.47 μm show that there is a strong sensitivity to the aerosol vertical distribution, including sensitivity to the aerosol layer top and base heights. We see in Figures 13a and 13b, that we need to increase the aerosol layer top height and also to detach the aerosol layer from the ground in the calculations in order to reduce the differences between measurements and simulations. The best solution is obtained for an aerosol layer located between 3.6 and 4.8 km with an AOT of 0.57 at 0.67 μm, r_g = 0.1 μm and m_r = 1.54. The second best solution is very close to the first one in terms of fitting accuracy (error term of 0.6 × 10^{-5} instead of 0.55 × 10^{-5}) and corresponds to an aerosol layer located between 2.4 and 4.8 km, an AOT of 0.69 at 0.67 μm, r_g = 0.1 μm and m_r = 1.54. The other solutions (i.e., other combinations of aerosol model and vertical structure) lead to error terms significantly larger (>10^{-5}) and are therefore rejected.

[61] In Figure 14, we show the polarized reflectance measured between 0.41 and 1.6 μm as a function of the scattering angle. The measured polarized reflectance exhibits an unusual spectral dependence, the signal increasing from 0.41 to 0.87 μm and then decreasing at 1.6 μm. This is explained by the fact that the contribution of the molecules below the aerosol layer is reduced by attenuation through the smoke plume. The fact that the measurements were acquired just above the aerosol layer also tends to minimize the contribution of molecules to the RSP measurements. The spectral dependence of the observed polarized reflectance is therefore determined by that of the aerosols. We include all the parameters of the fine mode in the retrieval process as well as the aerosol layer top height. Based on the LUT retrievals, the a priori value for the aerosol layer top height is set at 4.2 km with an a priori uncertainty of 0.6 km and the aerosol layer base height is fixed at an altitude of 3.6 km. We consider a spectrally flat refractive index and we do not include the coarse mode in the inversion. Potential modeling errors due to the neglect of the coarse mode particles are included in the total error covariance matrix. Figure 14 shows that the assumptions allowed a good fit to the measurements to be obtained. The convergence is achieved after five iterations. We obtain an AOT equal to 0.58 (0.01) at 0.67 μm, the retrieved effective radius and the variance are respectively equal to 0.165 μm (0.0015) and 0.25 (0.005), the real and imaginary refractive indices are equal to 1.505 (0.01) and 0.0315i (0.0015), respectively and P is equal to 560 hPa (Figure 10), corresponding to a height of 4.8 km. We retrieve a small effective radius and a high real refractive index, which is characteristic of the properties of the biomass burning particles [*Dubovik et al.*, 2002]. The retrieved imaginary refractive index leads to a single scattering albedo of 0.85 (0.005) at 0.55 μm. This value is rather similar to other estimates made for African savanna biomass burning particles (0.84< ω_0 < 0.88) [*Dubovik et al.*, 2002] and for fresh biomass burning particles observed in the vicinity of the source (0.86) [*Torres et al.*, 1998].

[62] Additional calculations show that there is a sensitivity of the retrievals to the aerosol layer base height. When we decrease the aerosol layer base height in the calculations, we observe an increase in the complex refractive index and AOT and a decrease of the particle size as well as a decrease of the fitting accuracy. For instance, when performing the retrieval with an aerosol layer base height of 2.4 km instead of 3.6 km, we found $\tau_{0.67}$ = 0.59, r_{eff} = 0.16 μm, m = 1.53 − 0.035i, P = 559 hPa and a single scattering albedo of 0.83. The fitting accuracy is only weakly reduced (0.2 × 10^{-6} instead of 0.15 × 10^{-6}). The fitting accuracy is significantly reduced (0.4 × 10^{-6} < error term < 10^{-5}) for aerosol layer base height smaller than 1.8 km. This indicates that the thickness of the aerosol layer must be less than 3 km in order to fit the measurements. The lidar measurements shown in Figure 12 suggest smaller thickness for the aerosol layer. This analysis shows that the aerosol layer base height cannot be accurately retrieved, but does affect the retrieved aerosol microphysical properties, and should therefore be considered as a nuisance factor that should be integrated over as part of any retrieval process. Assuming that the aerosol layer thickness is less than 2.4 km, we estimate the uncertainties in the retrieved parameters to be equal to 0.03 for $\tau_{0.67}$, 0.005 for r_{eff}, 0.02 for m_r and 0.003 for m_i.

[63] The AERONET Cimel Sun photometer located at the Rogers Dry Lake (RDL) station was the closest one to the flight track segment (≈80 km, see Figure 11). During the time when the RSP instrument flew (1930 to 2040 UT), the measured AOT varied between 0.2 and 0.7 at 0.67 μm. These

Table 6. Parameters in the Decomposition of the AERONET Cimel Spectral AOT Into a Cirrus Component and an Accumulation Mode With an Angstrom Power Law for the Four Measurements Surrounding the RSP Estimate

Data Source	Time (UT)	Total AOT	Cirrus AOT	Accumulation Mode AOT	Angstrom Power Law
AERONET	19:46	0.38	0.05	0.33	1.66
AERONET	19:52	0.44	0.08	0.38	1.66
RSP	20:01	0.56	0.00	0.56 (0.03)	1.73 (0.07)
AERONET	20:07	0.67	0.21	0.46	1.71
AERONET	20:22	0.71	0.10	0.61	1.62

data were however classified as cloud contaminated due to the presence of cirrus, although the smoke particle contribution probably dominated the optical depth, and for this reason no aerosol microphysical retrievals were performed. Observers in the aircraft noted that the data for which we have performed retrievals using RSP data were free of cirrus contamination but that cirrus was quite widespread. It is therefore reasonable, given the absence of any more detailed decomposition of the spectral AOT, to model the Cimel AOTs as being composed of cirrus and an accumulation mode that has a spectral AOT with a power law Angstrom dependence viz.,

$$\tau(\lambda) = \tau_{Cirrus} + \left(\frac{\lambda}{675}\right)^{-\alpha} \tau_{Acc}(675). \tag{24}$$

This simple model fits all the Cimel observations from 0.34 to 1.64 μm with an average absolute deviation of 0.02 that justifies the use of the power law exponent and accumulation mode optical depth as appropriate summary quantities to compare with the RSP retrievals. The primary reasons for using this decomposition are to reduce the impact of cirrus on the comparison and because aerosol microphysical properties (for which the Angstrom power law parameter is a proxy) typically vary less spatially and temporally than the aerosol burden and should therefore provide a better test of the validity of our retrieval than just looking at a single AOT. The AOT retrieved by the RSP (0.56 ± 0.03) is only within 0.1 of the Cimel accumulation mode AOT for the Sun photometer observation that is closest in time. However, the heterogeneity of the AOT and the distance between the RSP observation and the Cimel observation means that this difference is certainly within the observational uncertainty as can be seen by the rapid increase in accumulation mode AOT at RDL in the period after the RSP observations. For example, the Cimel AOT is 0.45 ± 0.12 if the standard deviation is estimated over the 40 minutes bracketing the polarimetric estimate. Although the accumulation mode AOT changed by 20% at RDL over the 15 minute period that brackets the RSP observations the Angstrom power law only changed by 3% in this time. The fact that our Angstrom power law retrieval 1.73 (0.07) agrees within the average of the Cimel values, 1.66 (0.04), within the combined uncertainty of the two estimates demonstrates the realism of our size distribution retrieval as does the fact that over the entire period summarized in Table 6 the difference between our retrieved Angstrom power law exponent and that estimated from the Cimel data is never more that 0.11.

[64] We have also calculated the TOMS aerosol index using the aerosol model and the vertical structure retrieved with the RSP instrument. We assume that the absorption properties retrieved in the visible part of the spectrum remain valid in the TOMS spectral bands (0.34–0.38 μm) and use a surface albedo of 0.05 for the calculations of the UV radiances. We calculated an Aerosol Index (AI) of 2.0 when the aerosol layer is assumed to lie between 3.6 and 4.8 km and an AI of 1.8 when the layer is assumed to lie between 2.4 and 4.8 km. If the thickness of the aerosol layer is reduced to 300 m similar to the smoke layers shown in Figure 12 the calculated AI is 2.3. The TOMS AI in the pixel that includes the location of our measurements is 3. Our measurements were however made on the southern edge of that pixel, with the pixel to the south being cloud contaminated. If we interpolate the TOMS AI to the location of our measurements using the surrounding values we obtain a TOMS AI value of 2.25. The good agreement between this interpolated TOMS AI value of 2.25 and the value predicted by our aerosol retrieval (assuming a 300 m aerosol layer) demonstrates that our aerosol retrieval is consistent with the TOMS AI within the range of uncertainty caused by the aerosol layer thickness. The agreement between the model calculated values and the TOMS AI product indicates that the vertical structure and single scattering albedo of our retrieval is consistent with spectral radiances observed in the UV.

6. Summary and Conclusions

[65] We have demonstrated that the polarization of light reflected by land surfaces can be represented sufficiently accurately for most purposes using a simple model constrained using the long wavelength (2.25 μm) measurements. Without such measurements errors in the assumed surface model will tend to dominate the retrieval [*Waquet et al.*, 2007], because only prior information is available to constrain the surface polarized reflectance. This surface model has been incorporated into an optimal estimation scheme for the determination of aerosol properties from polarimetric observations and was shown in a theoretical sensitivity analysis to provide a highly accurate estimate of the aerosol optical depth and microphysical model. This sensitivity analysis also showed the value of having short-wavelength polarimetric observations in order to estimate the vertical distribution of aerosols and the amount of light that aerosols absorb. Previous authors have noted the importance of errors caused by forward model assumptions [*Lebsock et al.*, 2007], but our analysis demonstrates that if a sufficient range of observations (spectrally and in terms of angular sampling) are available, the number of model assumptions can be reduced and the retrieval accuracy is indeed limited by the measurement accuracy, as indicated by more simplistic previous analyses [*Mishchenko and Travis*, 1997a].

[66] Our sensitivity study was then evaluated against the retrieval products provided by the analysis of Cimel sun/sky radiometer observations [*Dubovik and King*, 2000] and TOMS AI [*Torres et al.*, 1998]. At low AOT (<0.1) the differences between our retrievals of AOT and those from a

Cimel sunphotometer are 0.008 (0.01) for the AOT, 0.019 (0.008) μm for the effective radius and 0.02 (0.035) for the real refractive index where in each case the first number is the bias and the number in parentheses is the standard deviation. The only retrieved parameter where the discrepancy is larger than expected is the real refractive index and as we noted above this is also within the acceptable range of the combined uncertainties of the two estimates. These results demonstrate that even in pristine environments aerosol retrievals with the required accuracy [*Mishchenko et al.*, 2004] are possible using only polarized radiance observations provided a broad spectral range of measurements is available. This is in pronounced contrast to a previous analysis of the measurements available from POLDER where it was suggested that retrieval errors of 150% for AOT and refractive index were likely [*Lebsock et al.*, 2007]. At high AOT (>0.5) the lack of close spatial coincidence between the RSP aerosol retrievals and the Cimel sunphotometer, the cloud conditions and strong spatial gradients in the aerosol load make definitive validation of our aerosol retrievals we obtained over the smoke plumes problematic. We do however have consistency within the experimental uncertainties between our retrieval of AOT and Angstrom power law parameter and those estimated from Cimel observations. The calculated AI also agrees with the TOMS AI within the experimental uncertainties indicating that the vertical structure, aerosol single scattering albedo and AOT that we retrieved are at least a good predictor of UV radiances.

[67] Theoretical analysis and direct comparison to independent measurements demonstrate the capability of polarized radiance measurements to allow the retrieval of a detailed aerosol microphysical model and AOT over land surfaces. As we noted above, at high optical depths, the vertical structure of the aerosols acts as a nuisance parameter in the aerosol retrieval process, reducing the accuracy of the estimate of single-scattering albedo and AOT. The combination of polarization observations with simultaneous lidar observations, or high spectral resolution A-band radiometer observations, would therefore allow for more accurate aerosol retrievals under these conditions. The optimal estimation framework presented here allows that to be done quite easily and the planned launch of the NASA Glory APS into NASA's A-train constellation of satellites in June 2009 will allow this approach to be extended and applied to observations made by APS and the CALIPSO lidar, or the Orbiting Carbon Observatory A-band radiometer. An earlier opportunity to evaluate the combination of polarimetry, of the type analyzed here, and lidar observations will occur during the summer of 2008 when the RSP flies on the same aircraft as a High Spectral Resolution Lidar as part of the Arctic Research of the Composition of the Troposphere from Aircraft and Satellites field experiment that is part of the International Polar Year. As the results presented here demonstrate the use of aircraft data to evaluate and develop aerosol retrieval algorithms is invaluable.

Appendix A: Description of the Research Scanning Polarimeter

[68] The Research Scanning Polarimeter (RSP) was designed to collect data for atmospheric studies being conducted by NASA GISS and Columbia University science teams, and is the basis for the functional design of the Aerosol Polarimetry Sensor that is scheduled for launch as part of the NASA Glory mission in June of 2009.

[69] The RSP instrument uses a polarization compensated scan mirror assembly to scan the fields of view of six boresighted, refractive relay telescopes through ±60° from the normal with respect to the instrument base-plate. The refractive telescopes are paired, with each pair making measurements in three spectral bands. One telescope in each pair makes measurements of the two orthogonal polarization states at 0° and 90° to the meridional plane of the instrument while the other telescope simultaneously measures equivalent intensities for orthogonal polarization states at 45° and 135°. The orthogonal polarization states are spatially separated by a Wollaston prism and measured simultaneously on paired detectors. This approach ensures that the polarization signal is not contaminated by uncorrelated spatial or temporal scene intensity variations during the course of the polarization measurements, which could create "false" polarization. These measurements in each instantaneous field of view in a scan provide the simultaneous determination of the Stokes parameters I, Q and U in all nine spectral bands.

[70] The RSP has six spectral bands in the visible/near infrared (VNIR) that require four telescopes for the simultaneous measurements of I, Q and U. There are also two spectral bands in the Short-Wave Infra-Red (SWIR) blue enhanced silicon photodiodes are used to make measurements in six spectral bands at 410, 470, 555, 670, 865 and 960 nm. In the short wave infrared (SWIR) HgCdTe detectors cooled to 150K are used to make measurements in three spectral bands at 1590, 1880 and 2250 nm. The instantaneous field of view (14 mrad) of each telescope is scanned continuously with data being taken over a range of 120° (±60° from nadir) using a polarization-insensitive scan mirror system. This system consists of two mirrors each used at 45° angle of incidence and with their planes of incidence oriented orthogonally. This ensures that the polarization orientation that is perpendicular to the plane of reflection at the first mirror is parallel to the plane of reflection at the second mirror so that all polarization states are transmitted equally. The RSP also incorporates a calibration system that allows the relative responsivity of the detectors measuring orthogonal polarization states to be tracked allowing a polarimetric accuracy of better than 0.2% to be achieved independent of the scene that is being viewed.

Appendix B: Assumptions About Noise

[71] The absolute noise level is the same in Stokes parameters I, Q and U and it is given in reflectance unit by:

$$\sigma_{\varepsilon,i} = \frac{\sqrt{bR_i\mu_0}}{\mu_0}, \tag{B1}$$

where the coefficient b is determined from the optical throughput, detector quantum efficiency and preamplifier design primarily and it is verified against measurements. We use a value of b equal to 10^{-7}, which is a good approximation for the entire bands of the RSP instrument.

[72] The polarization ratio P is defined by:

$$P_i = \frac{R_{p,i}}{R_i}. \tag{B2}$$

[73] The errors on R_p then can be written as follows:

$$\Delta R_{p,i} = R_{p,i}\frac{\Delta R_i}{R_i} + \Delta P_i R_i. \tag{B3}$$

[74] From the equation above, we define the measurements errors due to the calibration uncertainty and polarimetric uncertainty as follows:

$$\begin{aligned} \sigma_{cal,i} &= R_{p,i}\tfrac{\Delta R_i}{R_i} \\ \sigma_{pol,i} &= \Delta P_i R_i \end{aligned}, \tag{B4}$$

where $\frac{\Delta R_i}{R_i}$ is the relative calibration uncertainty, which is fixed to 3%. ΔP is the polarimetric absolute accuracy which is calculated as follows:

$$\Delta P_i = 0.001 + 0.001 P_i. \tag{B5}$$

Appendix C: Radiometric Calibration of the RSP

[75] The RSP was calibrated on 25 September 2005 using a NIST traceable 1 kW FEL lamp operated in the manner prescribed by NIST so as to provide a calibrated irradiance that was reflected by a Spectralon plaque that also had NIST traceability of its reflectance. The NIST irradiances, that are provided with the FEL lamp at a standard set of wavelengths, were interpolated, using an initial fit to a blackbody spectrum as a method of prewhitening to reduce errors, to the 1-nm spectral grid of the RSP spectral response. These interpolated irradiances were then integrated over the spectral response of each band to produce an integrated estimate of the radiance that is observed by the RSP as the irradiance is reflected off the Spectralon plaque. It is these measurements that define the RSP radiance scale. The RSP radiances are then converted to a reflectance using a solar spectral irradiance provided by Judith Lean [*Lean*, 2000] that was also interpolated to the 1-nm grid and integrated over the response of each RSP band. It is this calibration that was used during the smoke measurements in October 2003. An additional calibration was performed using the Raytheon Santa Barbara Remote Sensing SIS2 integrating sphere over the spectral range from 350 to 1050 nm on 8 August 2005. This calibration showed a substantial change in calibration coefficients in the 410, 470 and 555 nm bands compared with that obtained on 25 September 2005. Subsequent analysis of the spectral variation of cloud reflectance, low altitude observations of sun glint and evaluation against the observed and simulated degree of linear polarization (which is independent of radiometric scale) have shown that the large change in calibration coefficients between 25 September 2005 and 8 August 2005 was erroneous and probably caused by errors in the calibration of the SIS2 which is only a tertiary radiance standard. However, it is this discrepancy between the radiance calibrations that causes us to ascribe a higher uncertainty to the radiometric accuracy of the shorter wavelength bands of the RSP.

[76] **Acknowledgments.** F. Waquet was supported as a postdoctoral fellow at NASA Goddard Institute for Space Studies by the NASA Glory Mission project. The participation of the RSP in ALIVE was funded by the NASA Radiation Sciences Program managed by Hal Maring. We would like to express our thanks to the National Aeronautics and Space Administration's Aerosol Robotic Network (AERONET) that supports and processes Cimel Sun Photometer data. The Cimel data that were used in our validation of ALIVE results were collected by the U.S. Department of Energy as part of the Atmospheric Radiation Measurement (ARM) Program Climate Research Facility (ACRF). The ARM Program is sponsored by the U.S. Department of Energy, Office of Science, Office of Biological and Environmental Research. The success of ALIVE was due to the hard work and dedicated efforts from a large team of scientists and engineers, Sky Research J-31, and Cessna pilots, crew, and support personnel, SGP site personnel, ARM infrastructure support, weather forecasters, and support from Greenwood aviation at Ponca City airport. We thank ARM for the support of this campaign. The flights over smoke in Southern California were funded by the Independent Program Office under the management of Steven Mango as part of the Coastal Stratocumulus Imposed Perturbation Experiment (CSTRIPE), and we acknowledge the assistance of Ron Ferek of the Office of Naval Research, John Seinfeld of California Institute of Technology and William Conant of the University of Arizona in facilitating our participation in CSTRIPE. The Cimel Sun Photometer Rogers Dry Lake, which is part of the AERONET, was used in validating our smoke retrievals. This instrument was mentored by Jeannette van den Bosch of NASA. The NASA GSFC CPL data, for which Matthew McGill is the Principal Investigator, was most informative in understanding the vertical structure of the smoke observations and was provided to us by Dennis Hlavka. Mike Fromm of the Naval Research Laboratory pointed out to us the value of the TOMS AI when looking at smoke from fires and provided the image shown here that was derived from data processed by the NASA GSFC Ozone Processing Team.

References

Abdou, W. A., D. J. Diner, J. V. Martonchik, C. J. Bruegge, R. A. Kahn, B. J. Gaitley, K. A. Crean, L. A. Remer, and B. Holben (2005), Comparison of coincident multiangle imaging spectroradiometer and moderate resolution imaging spectroradiometer aerosol optical depths over land and ocean scenes containing aerosol robotic network sites, *J. Geophys. Res.*, *110*, D10S07, doi:10.1029/2004JD004693.

Ackermann, J. (1998), The extinction-to-backscatter ratio of tropospheric aerosol: A numerical study, *J. Atmos. Oceanic Technol.*, *15*, 1043–1050.

Ackerman, T., and G. Stokes (2003), The atmospheric radiation measurement program, *Phys. Today*, *56*, 38–45.

Barnaba, F., and G. P. Gobbi (2004), Modeling the aerosol extinction versus backscatter relationship for lidar applications: Maritime and continental conditions, *J. Atmos. Oceanic Technol.*, *21*, 428–442.

Bodhaine, B., N. B. Wood, E. G. Dutton, and J. R. Slusser (1999), On Rayleigh optical depth calculations, *J. Atmos. Oceanic Technol.*, *16*, 1854–1861.

Bréon, F. M., D. Tanré, P. Leconte, and M. Herman (1995), Polarized reflectance of bare soils and vegetation: measurements and models, *IEEE Trans. Geosci. Remote Sens.*, *33*, 487–499.

Cairns, B., L. D. Travis, and E. E. Russell (1997), An analysis of polarization: Ground-based upward looking and aircraft/satellite based downward looking measurements, *Proc. SPIE Int. Soc. Opt. Eng.*, *3220*, 103–114.

Cairns, B., L. D. Travis, and E. E. Russell (1999), The research scanning polarimeter: Calibration and ground-based measurements, *Proc. SPIE*, *3754*, 186–197.

Cairns, B., et al. (2001), Aerosol retrievals over land surfaces: The advantages of polarization, paper presented at the AMS Annual Meeting, Albuquerque, NM, January.

Cattrall, C., J. Reagan, K. Thome, and O. Dubovik (2005), Variability of aerosol and spectral lidar and backscatter and extinction ratios of key aerosol types derived from selected aerosol robotic network locations, *J. Geophys. Res.*, *110*, D10S11, doi:10.1029/2004JD005124.

Chowdhary, J., B. Cairns, M. I. Mishchenko, and L. D. Travis (2001), Retrieval of aerosol properties over the ocean using multispectral and multiangle photopolarimetric measurements from the research scanning polarimeter, *Geophys. Res. Lett.*, *28*, 234–246.

Chowdhary, J., B. Cairns, and L. Travis (2002), Case studies of aerosol retrievals from multiangle, multi-spectral photo-polarimetric remote sensing data, *J. Atmos. Sci.*, 383–397.

Chowdhary, J., B. Cairns, and L. D. Travis (2006), Contribution of water-leaving radiances to multiangle, multispectral polarimetric observations over the open oceans: Bio-optical model results for case I waters, *Appl. Opt.*, *45*, 5542–5567.

Chu, D. A., Y. J. Kaufman, C. Ichoku, L. A. Remer, D. Tanré, and B. N. Holben (2002), Validation of MODIS aerosol optical depth retrieval over land, *Geophys. Res. Lett.*, *22*(12), 8007, doi:10.1029/2001GL013205.

Chung, S. H., and J. H. Seinfeld (2005), Climate response of direct radiative forcing of anthropogenic black carbon, *J. Geophys. Res.*, *110*, D11102, doi:10.1029/2004JD005441.

D'Almeida, G. A., P. Koepke, and E. P. Shettle (1991), *Atmospheric Aerosols: Global Climatology and Radiative Characteristics*, 561 pp., A Deepak Publishing, Hampton, VA.

Deschamps, C., et al. (1994), The POLDER mission: Instrument characteristics and scientific objectives, *IEEE Trans. Geosci. Remote Sens.*, *32*, 598–615.

De Haan, J. F., P. B. Bosma, and J. W. Hovenier (1987), The adding method for multiple scattering calculations of polarized light, *Astron. Astrophys.*, *183*, 371–391.

Deuzé, C., et al. (2001), Remote sensing of aerosols over land surfaces from POLDER-ADEOS-1 polarized measurements, *J. Geophys. Res.*, *106*, 4913–4926.

Dubovik, O., and M. D. King (2000), A flexible inversion algorithm for retrieval of aerosol optical properties from Sun and sky radiance measurements, *J. Geophys. Res.*, *105*, 20,673–20,696.

Dubovik, O., et al. (2002), Variability of absorption and optical properties of key aerosol types observed in worldwide locations, *J. Atmos. Sci.*, *59*, 590–608.

Elias, T., B. Cairns, and J. Chowdhary (2004), Surface optical properties measured by the airborne research scanning polarimeter during the CLAMS experiment, in *Remote Sensing of Clouds and the Atmosphere VIII*, edited by K. P. Schäfer et al., *Proc. SPIE*, *5235* (#79), pp. 595–606, SPIE, Bellingham, WA.

Flowerdew, R. J., and J. D. Haigh (1995), An approximation to improve accuracy in the derivation of surface reflectances form multi-look satellite radiometers, *Geophys. Res. Lett.*, *22*, 1693–1696.

Grant, L., C. S. T. Daughtry, and V. C. Vanderbilt (1993), Polarized and specular reflectance variation with leaf surface features, *Physiol. Plant.*, *88*, 1–9, doi:10.1111/j.1399-3054.tb01753.x.

Hansen, J. E., and L. D. Travis (1974), Light scattering in planetary atmospheres, *Space Sci. Rev.*, *16*, 527–610.

Hansen, J., et al. (2005a), Efficacy of climate forcings, *J. Geophys. Res.*, *110*, D18104, doi:10.1029/2005JD005776.

Hansen, J., et al. (2005b), Earth's energy imbalance: Confirmation and implications, *Science*, *308*(5727), 1431–1435, doi:10.1126/science.1110252.

Hasekamp, O. P., and J. Landgraf (2007), Retrieval of aerosol properties over land surfaces: Capabilities of multiple-viewing-angle intensity and polarization measurements, *Appl. Opt.*, *46*(16), 3332–3344, doi:10.1364/AO.46.003332.

Haywood, J. M., and K. P. Shine (1995), The effect of anthropogenic sulfate and soot on the clear-sky planetary radiation budget, *Geophys. Res. Lett.*, *22*, 603–606.

Herman, J. R., P. Bhartia, O. Torres, C. Hsu, C. Seftor, and E. Celarier (1997), Global distribution of UV-absorbing aerosol from Nimbus-7/TOMS data, *J. Geophys. Res.*, *102*, 16,911–16,922.

Hlavka, D., S. P. Palm, W. D. Hart, J. D. Spinhirne, M. J. McGill, and E. J. Welton (2005), Aerosol and cloud optical depth from GLAS: Results and verification for an October 2003 California fire smoke case, *Geophys. Res. Lett.*, *32*, L22S07, doi:10.1029/2005GL023413.

Hoff, R. M., S. P. Palm, J. A. Engel-Cox, and J. D. Spinhirne (2005), GLAS long-range transport observation of the 2003 California forest fire plumes to the northeast US, *Geophys. Res. Lett.*, *32*, L22S08, doi:10.1029/2005GL023723.

Hsu, N. C., S.-C. Tsay, M. D. King, and J. R. Herman (2004), Aerosol properties over bright-reflecting source regions, *IEEE Trans. Geosci. Remote Sens.*, *42*(3), 557–559, doi:10.1109/TGRS.2004.824067.

Intergovernmental Panel on Climate Change 2007, et al. (2007), Changes in atmospheric constituents and in radiative forcing, in *Climate Change 2007: The Physical Science Basis. Contribution of Working Group I to the Fourth Assessment Report of the Intergovernmental Panel on Climate Change*, edited by S. Solomon et al., pp. 129–234, Cambridge Univ. Press, Cambridge, U.K.

Kaufman, Y. J., D. Tanre, T. Nakajima, J. Lenoble, R. Frouin, H. Grassl, B. M. Herman, M. D. King, and P. M. Teillet (1997a), Passive remote sensing of tropospheric aerosol and atmospheric correction for the aerosol effect, *J. Geophys. Res.*, *102*, 16,815–16,830.

Kaufman, Y. J., et al. (1997b), The MODIS 2.1 μm channel—Correlation with visible reflectance for use in remote sensing of aerosol, *IEEE Trans. Geosci. Remote Sens.*, *35*, 1286–1298.

Kaufman, Y. J., N. Gobron, B. Pinty, J.-L. Wildlowski, and M. M. Verstraete (2002), Relationship between surface reflectance in the visible and mid-IR used in MODIS aerosol algorithm: Theory, *Geophys. Res. Lett.*, *29*(3), 2116, doi:10.1029/2001GL014492.

Kahn, R., P. Banerjee, and D. McDonald (2001), Sensitivity of multi-angle imaging to natural mixtures of aerosols over ocean, *J. Geophys. Res.*, *106*, 18,219–18,238.

Kahn, R. A., B. J. Gaitley, J. V. Martonchik, D. J. Diner, K. A. Crean, and B. Holben (2005), Multiangle imaging spectroradiometer (MISR) global aerosol optical depth validation based on 2 years of coincident aerosol robotic network (AERONET) observations, *J. Geophys. Res.*, *110*, D10S04, doi:10.1029/2004JD004706.

Keeley, J. E. (2004), Fire management of Califonia shrubland landscapes: Lessons from the October 2003 wildfires in Southern California, *J. For.*, *102*(7), 26–31, doi:10.1007/s00267-001-0034-Y.

King, M. D., et al. (1978), Aerosol size distributions obtained by inversion of spectral optical depth measurements, *J. Atmos. Sci.*, *35*, 2153–2167.

Lacis, A. A., and V. Oinas (1991), A description of the correlated k distribution method for modeling nongray gaseous absorption, thermal emission and multiple scattering in vertically inhomogeneous atmospheres, *J. Geophys. Res.*, *96*, 9027–9063.

Lean, J. (2000), Evolution of the Sun's spectral irradiance since the Maunder minimum, *Geophys. Res. Lett.*, *27*, 2425–2428.

Lebsock, M. D., T. S. L'Ecuyer, and G. L. Stephens (2007), Information content of near-infrared spaceborne multiangular polarization measurements for aerosol retrieval, *J. Geophys. Res.*, *112*, D14206, doi:10.1029/2007JD008535.

Lohmann, U., and J. Feichter (2005), Global indirect aerosol effects: A review, *Atmos. Chem. Phys.*, *5*, 715–737, 2005, http://www.atmos-chem-phys.net/5/715/2005/.

Martonchik, J., et al. (1998), Techniques for the retrieval of aerosol properties over land and ocean using multiangle imaging, *IEEE Trans. Geosci. Remote Sens.*, *36*, 1212–1227.

Martonchik, J. V., D. J. Diner, K. A. Crean, and M. A. Bull (2002), Regional aerosol retrieval results from MISR, *IEEE Trans. Geosci. Remote Sens.*, *40*, 1520–1531.

Martonchik, J. V., D. J. Diner, R. Kahn, B. Gaitley, and B. N. Holben (2004), Comparison of MISR and AERONET aerosol optical depths over desert sites, *Geophys. Res. Lett.*, *31*, L16102, doi:10.1029/2004GL019807.

Mishchenko, M. I., and L. D. Travis (1997a), Satellite retrieval of aerosol properties over the ocean using measurements of reflected sunlight: Effect of instrumental errors and aerosol absorption, *J. Geophys. Res.*, *102*, 13,543–13,553.

Mishchenko, M. I., and L. D. Travis (1997b), Satellite retrieval of aerosol properties over the ocean using polarization as well as intensity of reflected sunlight, *J. Geophys. Res.*, *102*, 16,989–17,013.

Mishchenko, M. I., L. D. Travis, and A. A. Lacis (2002), *Scattering, Absorption and Emission of Light by Small Particles*, Cambridge Univ. Press, Cambridge.

Mishchenko, M. I., B. Cairns, J. E. Hansen, L. D. Travis, R. Burg, Y. J. Kaufman, J. V. Martins, and E. P. Shettle (2004), Monitoring of aerosol forcing of climate from space: analysis of measurement requirements, *J. Quant. Spectrosc. Radiat. Transfer.*, *88*, 149–161, doi:10.1016/.jqsrt.2004.03030.

Mishchenko, M. I., et al. (2007), Precise and accurate monitoring of terrestrial aerosols and total solar irradiance: Introducing the Glory mission, *Bull. Amer. Meteorol. Soc.*, *88*, 677–691, doi:10.1175/BAMS-88-5-677.

Mühle, J., T. J. Lueker, Y. Su, B. R. Miller, K. A. Prather, and R. F. Weiss (2007), Trace gas and particulate emissions from the 2003 southern California wildfires, *J. Geophys. Res.*, *112*, D03307, doi:10.1029/2006JD007350.

Nadal, F., and F. M. Bréon (1999), Parameterization of surface polarized reflectances derived from POLDER spaceborne measurements, *IEEE Trans. Geosci. Remote Sens.*, *37*, 1709–1719.

North, P. R. J. (2002), Estimation of aerosol opacity and land surface bidirectional reflectance from ATSR-2 dual-angle imagery: Operational method and validation, *J. Geophys. Res.*, *107*(D12), 4149, doi:10.1029/2000JD000207.

Pollack, J. B., O. B. Toon, and B. N. Khare (1973), Surface refractive index, *Icarus*, *19*, 372–389.

Ramanathan, V., et al. (2001), Aerosols, climate, and the hydrological cycle, *Science*, *294*, 2119–2124.

Remer, L. A., et al. (2005), The MODIS aerosol algorithm, products and validation, *J. Atmos. Sci.*, *62*, 947–973.

Rodgers, C. D. (2000), *Inverse Methods for Atmospheric Sounding*, 238 pp., World Sci., Hackensack, N. J.

Rosenzweig, C., et al. (2008), Attributing physical and biological impacts to anthropogenic climate change, *Nature*, *453*, 353–357, doi:10.1038/nature06937.

Russell, P. B., J. M. Livingston, P. Hignett, S. Kinne, J. Wong, A. Chien, R. Bergstrom, P. Durkee, and P. V. Hobbs (1999), Aerosol-induced

radiative flux changes off the United States mid-Atlantic coast: Comparison of values calculated from sunphotometer and in situ data with those measured by airborne pyranometer, *J. Geophys. Res.*, *104*, 2289–2307.

Schmid, B., et al. (1997), Retrieval of optical depth and particle size distributions of tropospheric and stratospheric aerosols by means of sun photometry, *IEEE Trans. Geosci. Remote Sens.*, *35*, 172–181.

Schmid, B., et al. (2003), Column closure studies of lower tropospheric aerosol and water vapor during ACE-Asia using airborne Sun photometer and airborne in situ and ship-based lidar measurements, *J. Geophys. Res.*, *108*(D23), 8656, doi:10.1029/2002JD003361.

Stamnes, K., W. Li, B. Yan, H. Eide, A. Barnard, W. S. Pegau, and J. J. Stamnes (2003), Accurate and self-consistent ocean color algorithm: Simultaneous retrieval of aerosol optical properties and chlorophyll concentrations, *Appl. Opt.*, *42*, 939–951.

Tanré, D., M. Herman, and Y. J. Kaufman (1996), Information on aerosol size distribution contained in solar reflected radiances, *J. Geophys. Res.*, *101*, 19,043–19,060.

Torres, O., P. K. Bhartia, J. R. Herman, Z. Ahmad, and J. Gleason (1998), Derivation of aerosol properties from satellite measurements of backscattered ultraviolet radiation: Theoretical basis, *J. Geophys. Res.*, *103*, 17,099–17,110.

Torres, O., P. K. Bhartia, J. R. Herman, A. Sinyuk, P. Ginoux, and B. Holben (2002), A long-term record of aerosol optical depth from TOMS observations and comparison to AERONET measurements, *J. Atmos. Sci.*, *59*, 398–413.

Veefkind, J. P., G. D. de Leeuw, and P. A. Durkee (1998), Retrieval of aerosol optical depth over land using two-angle view satellite radiometry during TARFOX, *Geophys. Res. Lett.*, *25*, 3135–3138.

Waquet, F., P. Goloub, J.-L. Deuzé, J.-F. Léon, F. Auriol, C. Verwaerde, J.-Y. Balois, and P. François (2007), Aerosol retrieval over land using a multiband polarimeter and comparison with path radiance method, *J. Geophys. Res.*, *112*, D11214, doi:10.1029/2006JD008029.

Zagolski, F., N. T. O'Neill, A. Royer, and J. R. Miller (1999), Validation of a DDV-based aerosol optical depth retrieval algorithm using multialtitude spectral imagery, *J. Geophys. Res.*, *104*, 27,959–27,971.

B. Cairns, M. I. Mishchenko, and L. D. Travis, NASA Goddard Institute for Space Studies, 2880 Broadway, New York, NY 10025, USA.

J. Chowdhary and K. Knobelspiesse, Department of Applied Physics and Applied Mathematics, Columbia University, 2880 Broadway, New York, NY 10025, USA.

B. Schmid, Pacific Northwest National Laboratory, 902 Battelle Boulevard, P.O. Box 999, MSIN K9-24, Richland, WA 99352, USA.

F. Waquet, Laboratoire d'Optique Atmosphérique, Université des Sciences et Technologies de Lille, F-59655 Villenueve d'Ascq, France. (waquet@ loa.univ-lille1.fr)